

Normal Stiffness of Multiscale Rough Surfaces in Elastic Contact

vorgelegt von
Dipl.-Ing. Roman Pohrt
aus Berlin

von der
Fakultät V Verkehrs- und Maschinensysteme
der Technischen Universität Berlin
zur Erlangung des akademischen Grades
Doktor der Ingenieurwissenschaften (Dr.-Ing)
genehmigte Dissertation

Promotionsausschuss

Vorsitzender: Prof. Dr.-Ing. C.O. Paschereit

Gutachter: Prof. Dr. rer. nat. V. Popov

Prof. Dr.-Ing. M. Paggi

Tag der wissenschaftlichen Aussprache: 16. Dezember 2013

Berlin 2013

D 83

Preface

The present work was conducted at the *Fachgebiet Systemdynamik und Reibungsphysik* of *Technische Universität Berlin* chaired by Prof. Valentin L. Popov. He was very actively involved in all the findings and the countless discussion with him were invaluable to me. I wish to thank him for being a very enthusiastic advisor and for conveying his personal philosophy and style of research (“*You should always expect dimensionless constants to be of the order of unity.*”). His stimulus and inquisitiveness were crucial in obtaining the (mostly theoretical) results presented here.

I also wish to thank my colleagues, in particular Jasminka Starcevic for her positivity and support, Birthe Grzempa for her assistance and patience, Robbin Wetter for his willingness to discuss anything upcoming spontaneously, Johannes Thaten for both his technical expertise and his relaxed attitude and Silvio Kürschner for going through the pain of debugging different relaxation schemes with me. I also appreciated the valuable discussions I had with Pawel Podsiadlo in the lab of Prof. Stachowiak. He was the one who inspired the major finding of $\alpha = (H + 1)^{-1}$ after we had agonized for months about the provenance of the power-law.

Abstract – English

Engineering surfaces are rough. When two rough surfaces are brought into contact by applying a normal force, these surfaces will deform in the vicinity of the opposing top peaks (asperities). For both theoretical understanding and analysis the indentation of fractal rough surfaces has caught researchers' interest. These surfaces include roughness features at multiple length scales, possibly ranging from nanometers to meters. The actual indentation process can be characterized by the dependency of the contact stiffness on the applied normal force.

In the past, researchers have suggested a general power-law dependency using different analytical and numerical approaches. For examples, advanced multi-asperity-models including elastic interaction suggested an exponent between 0.6 and 1. According to the diffusion theory by Bo Persson, the dependence should be linear, thus have the exponent 1. The discrepancy between different approaches has not been entirely resolved.

The present work introduces numerical results obtained by means of the boundary element method and finds a power-law behavior. A clear dependency of the exponent on the Hurst exponent is found and described quantitatively. Studies conducted with the method of dimensionality reduction confirm these results.

Special insight is given by the derivation of an analytical formula describing this dependency. It is based mainly on the analogy between a fractal roughness and rotational symmetric indenter shape. The indentation of the latter had been solved in the 1950s and 60s by Galin/Sneddon.

The results obtained in this thesis are applied to nominally flat and curved surfaces, where closed-form solutions are found.

Zusammenfassung – German

Technische Oberflächen sind rau. Werden zwei raue Oberflächen mittels wirkender Normalkraft zusammengebracht, so werden Sie sich in der Nähe der Rauheitsspitzen (Asperiten) deformieren und so ihre Form angleichen. Zum theoretischen Verständnis der Kontaktmechanik ist das elastische Eindruckverhalten fraktaler Oberflächen von großem Interesse. Solche Oberflächen besitzen Rauheiten auf mehreren Skalen, ggf. von Nanometern bis Metern. Der Eindruckvorgang kann beschrieben werden durch die Abhängigkeit der Kontaktsteifigkeit von der wirkenden Normalkraft.

In der Vergangenheit wurde hierfür durch verschiedene theoretische und numerische Ansätze allgemein eine Potenzabhängigkeit vorgeschlagen. So ergaben verbesserte Asperitenmodelle mit elastischer Interaktion Exponenten zwischen 0.6 und 1. Die Diffusionstheorie nach Bo Persson, angewendet auf *nominell glatte* fraktale Oberflächen, ergibt eine lineare Abhängigkeit, entsprechend Exponent 1. Die Diskrepanz zwischen den verschiedenen Ansätzen ist bisher nicht geklärt worden.

Die hier präsentierte Arbeit behandelt das Problem ebenfalls numerisch mit Hilfe der Randelementemethode und findet eine Potenzabhängigkeit. Dabei wird eine Abhängigkeit des Exponenten vom geometrischen Rauheitsparameter Hurst Exponent festgestellt und diese quantifiziert. Es werden auch Studien mit der Methode der Dimensionsreduktion durchgeführt, mit gleichem Ergebnis.

Eine besondere Erkenntnis stellt die Herleitung einer analytischen Formel zur Beschreibung der o.g. Abhängigkeit dar. Sie wird im Wesentlichen erreicht durch Herstellen einer Analogie zum Eindruckverhalten eines rotationssymmetrischen Indenters, wie es bereits in den 1950er/60er Jahren von Galin/Sneddon gelöst wurde.

Die hier neu gewonnenen Erkenntnisse werden auf makroskopisch glatte und gekrümmte Oberflächen angewendet, wobei geschlossene Lösungen gefunden werden.

Contents

1	Introduction	1
2	Description of surface roughness	3
2.1	Measuring real surface roughness	4
2.1.1	Mechanical methods	4
2.1.2	Optical methods	5
2.2	Fractal roughness - a generalized model	7
2.3	Numerical surface generation	9
2.3.1	Random Midpoint Algorithm (RMA)	10
2.3.2	Inverse Fourier Transform (IFT)	12
3	Contact models	15
3.1	Greenwood and Williamson	15
3.2	Persson	18
4	Normal contact stiffness	22
4.1	Geometric properties of the contact stiffness	24
4.2	Dimensionless variables	25
4.3	Bounds on the assumptions	27
4.4	Analytical estimation	29
4.4.1	Power-Law dependence in a simple fractal model	30
4.4.2	Implementation to random rough surfaces	32
4.5	Simulation	38
4.5.1	3D Boundary Element Method (BEM)	38
4.5.2	Method of Dimensionality Reduction (MDR)	39
4.5.3	Comparison numerical and analytical	45
4.6	Comparison to previous models	49
5	Applications	52
5.1	Application to nominally flat fractal surfaces	52
5.2	Application to curved bodies	53
6	Conclusion	58
7	Outlook	59

A Appendix	62
A.1 BEM	62
A.1.1 Formulation for different geometric scenarios	65
A.1.2 Fast integration techniques	73
A.1.3 Iterative procedures	78
A.2 1D Method of Dimensionality Reduction	80
References	86

Symbols

Symbols using Latin letters

symbol	dimension	quantity	definition
a	m	contact radius	
A	m ²	real contact area	
\bar{A}	m ²	dimensionless real contact area	$\frac{A}{A_0}$
A_0	m ²	apparent contact area	
B_{1D}	m	1D amplitude spectrum	
B_{2D}	m	3D amplitude spectrum	
$const$	1	constant	
C_{1D}	m ³	1D power spectrum	
C_{2D}	m ⁴	3D power spectrum	
d	m	diameter / indentation depth	
D_f	1	fractal dimension	$D_f = 3 - H$
E	Pa	modulus of elasticity	
E^*	Pa	reduced modulus of elasticity	$\left(\frac{1-\nu_1}{E_1} + \frac{1-\nu_2}{E_2}\right)^{-1}$
F_N, F	N	(Normal) Force	
\bar{F}	1	dimensionless normal Force	see eq. 4.13
h	m	surface topography / rms roughness	
H	1	Hurst Exponent	see eq. 2.1
H_v	1	Heaviside function	
k_N	Nm ⁻¹	normal stiffness	
k_t	Nm ⁻¹	tangential stiffness	
\bar{k}	1	dimensionless normal stiffness	see eq. 4.8
K	Nm ⁻¹	interfacial stiffness	
$K_{ij\hat{i}\hat{j}}$	1	influence factors	see eq. A.15
L	m	macroscopic system length	$\sqrt{A_0}$
N	1	no. of grid points / total asperity no.	
p	Pa	pressure	
q	m ⁻¹	wave number	
q_{min}, q_{max}	m ⁻¹	minimum / maximum wave number	
q_0	m ⁻¹	minimal system wave number	$2\pi/L$
\bar{q}	m ⁻¹	wave vector	
r	m	radius	

R	m	effective radius of curvature
u_0	m	characteristic height
U_{el}	J	elastic energy
x,y,z	m	spatial coordinates
Z	m	vertical range
∇z	1	mean surface slope

Symbols using Greek letters

symbol	dimension	quantity	definition
α	1	exponent	
Δ	m	grid spacing	$\Delta = L/N-1$
Φ	1	probability density	
λ	m	wavelength	
λ	1	magnification	
λ	m^{-1}	rate parameter in height distribution	
Λ_e	S	electrical conductivity	
Λ_t	WK^{-1}	thermal conductivity	
ν	1	Poisson's ratio	
μ	1	Coefficient of Friction	$\frac{F_{friction}}{F_{normal}}$
ϕ	1	phase angle, height distribution	
ρ	Sm^{-1}	electric resistivity	
σ_0	Pa	hardness	
σ_k, σ_F	Nm^{-1}	standard deviation of k or F	
Ψ	1	Plasticity index	

Remark on 'Dimensions'

In the course of this work, two different terms 'dimension' will be used. Whenever the topological description of the surface is treated, the term refers to the *fractal* dimension of the surface, which ranges from 2 to 3. In the context of simulations, a *one-dimensional* calculation is obtained by means of the Method of Dimensionality Reduction (MDR), while the Boundary Element calculations are referred to as *three-dimensional*.

1 Introduction

This present work deals with the dry contact problem of rough surfaces. The basic setup consists of two elastic bodies with some kind of textured surface that are pressed together. Due to the roughness features, the bodies will only come into real material contact in the vicinity of the top caps, so called asperities. The true area of contact in many relevant cases is only a minor fraction of the apparent contact area.

This fact is of utmost importance for basically all aspects of contact mechanics, e.g. the current distribution of contact spots governs the electrical and heat conductivity, the lateral load bearing capacity, the sound reflection properties, the friction force, the adhesive force, the lateral and normal stiffness of the contact. Some of these are actually closely related and this work initially focuses on the normal contact stiffness.

In analytical contact mechanics, starting with the very basic work of Hertz [31], a set of assumptions is often used in order to simplify the analysis:

half-space-approximation: low slopes, in the case of normal contact, both rough surfaces can be reduced to one effective roughness and a smooth counterpart, one of which is assumed to be rigid

frictionless contact: only normal stresses arise

perfect linear elasticity: plasticity is not taken into account

Even with these simplifying assumptions, solving the contact problem for a given surface pairing is not a trivial thing to do. The two main problems are the following:

- all asperities influence each other via the elastic coupling
- the true area of contact is not known

Not knowing the real area of contact in advance is an issue, because the problem demands for special boundary conditions to be fulfilled in both the region of contact and of no-contact. Whenever we assume a specific spot to be in contact, the gap between the two bodies must vanish and, in a non-adhesive contact, there must be a positive pressure. In contrast, whenever the surfaces are not in intimate contact, a positive gap width and a vanishing pressure is required. Negative gap widths are never allowed.

In the past, different models were proposed in order to approach the problem for non-smooth surfaces. The most influential one is by Greenwood and Williamson (GW) [26]. Its success is partly due to its simplicity and the very charming fact that it is the first

model to predict the real area of contact to rise linearly with the applied load [32][33][12]. This very basic model has inspired many modifications. In recent works these models are often criticized, because they do not take into account the elastic coupling between asperities. The basic Greenwood-Williamson-model assumes all the tops peaks to have the same radius of curvature but at different heights. This means that the corresponding power-spectrum of the surface is narrow-banded. It has a characteristic wavelength. In contrast this current work focuses on self-affine surfaces which are characterized by the fact, that roughness amplitudes from a multitude of wavelengths play a dominant role. These surfaces have become a hot topic in tribology over the last years [6][13][35][85]. The main objective of this work is to investigate the indentation behavior of elastic, self-similar surfaces while taking into account the elastic coupling. This behavior is described in terms of a force/indentation-dependence. More specifically, the contact stiffness defined as the derivative of the normal force with respect to the indentation depth will be considered, because it can be related directly to many relevant quantities, see sec. 4. The basic methodologies used are analytical analysis and simulation employing both the Boundary Element Method (BEM) and the Method of Dimensionality Reduction (MDR).

The results of this work strongly suggest that

- It is of great importance whether or not a surface has a characteristic wavelength.
- When no characteristic wavelength exists, the contact behavior can successfully be described using the ideas developed in this work and its preceding publications.
- In many cases involving a characteristic wavelength, the assumptions of the GW-model are indeed reasonable.

In the next chapter 2, an introduction to the description of rough 3D-surfaces will be given with focus on self-affine roughness features. Chapter 3 will review the most influential contact models so far and point out their fundamental differences. The indentation of rough surfaces will be the subject of chapter 4, where it will be shown why the *contact stiffness* can be seen as the key property in contact mechanics. The most important findings of this work will be presented in 4.4.1 as a theoretical foundation to go along with the numerical investigations presented 4.5. Needless to say that in the process of shedding light into this area of research, the numerics actually preceded our analytical insights.

2 Description of surface roughness

A surface topography can be seen as a mapping of the vertical height z onto one or two lateral coordinates. For determining the roughness, the point of origin is usually not of interest and the reference height can be chosen arbitrarily as well, e.g. the lowest values appearing or the overall mean value. In measurement engineering it is often requested that there is no overhang or cavity existing in the surface topography. This is a reasonable assumption for most technical surfaces on the relevant scales. Furthermore, in the theoretical and numerical part of this work, we will always assume the half-space-approximation, thereby demanding for the surface slope to be low – an even stricter requirement.

If the roughness is defined as the divergency from the perfectly smooth shape specified in a technical drawing, it can be subdivided according to the lengthscale that is of interest. The DIN 4760 standard defines 6 classes of deviance:

- deviation in shape and position
- waviness
- roughness in the form of groove marks
- roughness in the form of rills, spills, knolls
- microstructure
- lattice arrangement

From a tribological point of view, all of these classes are of interest in addition to the macroscopic shape, because it is their interplay that governs many processes in contact mechanics and friction. When using a fractal model of the surface roughness, it must be specified what orders are to be included in the model. For example, rocks or fractured surfaces may inherit a fractal behavior for even the longest scale, which is the sample length itself, as opposed to machined surfaces that appear smooth on the macroscopic scale. Any topography obtained from measurement will be limited in the scales that are considered. Classical tactile systems are limited on the small scale by the radius of the tip (see sec. 2.1.1) and optical systems have a lateral resolution which is defined by the smallest wavelength that is used.

As surface measurements often treat only a small local sample, they cannot detect roughness feature longer than that particular sample, thereby imposing a technical bound on

the roughness scale. We will see in sec. 2.1 that no single measurement can successfully describe the entire roughness spectrum for technical relevant surfaces, but from combining different methods, it was found that there is indeed a model that can accurately describe the roughness features in multiple length scales [56]. This *fractal model* will be covered in sec. 2.2.

2.1 Measuring real surface roughness

Obtaining the surface topography of a given physical sample is not always a simple task. There is a multitude of machines on the market that can be used but whether or not a particular instrument or even measurement principle is suitable for the specific sample depends on several aspects.

- the minimum and maximum wavelength to be included in the measurement
- the vulnerability of the material to mechanical deformation and/or wear
- accessibility of the surface sample, location within the component
- amplitude of the roughness

There are 3 basic classes of measurement devices

- acoustic
- mechanical (tactile)
- optical

In practice, only the last two are used in tribology.

2.1.1 Mechanical methods

In mechanical devices, a tip is brought into contact with the surface and moved laterally. A small normal force is applied so that the tip follows closely the topography. Great accuracy can be achieved with such devices. Roughness features with an amplitude of about $1\ \mu\text{m}$ can be detected. Mechanical measuring of the surface roughness is widely used in industrial applications and has inspired the definition of many standards concerning the quality of a machined surface, polishing etc [79], [49].

There are three major drawbacks with mechanical sensing of the roughness. First, no soft materials can be tested, because the tip will either deform the body or penetrate it,

so the results will be falsified. Second, the data rate is limited. Due to inertia effects, only a few samples can be obtained per second. Furthermore the procedure works one-spot-at-a-time, so it easily becomes a lengthy process, sensing a 3D surface. Third, the lateral resolution is limited. When a ruby sphere is used as a tip, its diameter dictates the smallest wavelength that can be detected. Typical values of the diameter are $d \geq 0.1$ mm

2.1.2 Optical methods

In contrast to mechanical methods, optical devices avoid most of the restrictions mentioned above. They work free of contact, have a high data rate and achieve a great lateral and vertical resolution. A good overview of the optical principles can be found in [30], as well as references to literature covering the topic in more detail. The most common principles will be briefly summarized below.

Optical interferometry

The basic principle of interferometry is to superpose two light beams – one reference wave with known phases and one wave being reflected from the object. From the coherence between the two, one can deduce the phases of the object wave and finally calculate the objects shape. This type of measurement is extremely precise, giving vertical resolution up to 0.1 nm, which is in the order of atoms. Unfortunately the surface has to be optically smooth, or else there will be speckle appearing. This statistical phenomenon arises from the superposition of many elementary wave fronts having random phases. As the object wave is superposed in that way, it cannot easily be reconstructed. Several possibilities have been proposed to overcome this problem. For example, one can use longer wavelengths, thereby effectively smoothing the surface. Employing longer waves also increases the range of unambiguousness, because measurements based on interferometry are generally only unique in a range of half the wavelength, which will usually be only a few hundred nm [30].

Optical focus-search

Focus-search methods are based on the fact that a proper optical projection is only possible in a specific plane. Knowing the optical system, one can deduce the position of the reflecting point. In the easiest setup, a light spot is projected onto the surface and its reflection is directed towards a pinhole and a detector. The optical system is then refocused mechanically until the intensity at the detector reaches a maximum, that

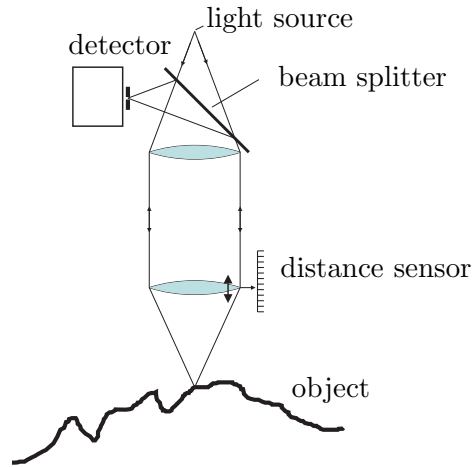


Figure 1: The basic principle of focus-search based surface measurement. The lower lens is displaced until the light spot is in focus. The distance between the lower lens and the point on the rough surface is constant (the focal length), so the height of the material point is directly correlated to the optimum position of the lower lens.

is until the projection of the light spot is sharp. In this simple setup, all 3 directions have to be tested in a serial order, which is time-consuming. Recent scanning microscopes are able to determine the focus spot for many points in the x - y -plane in parallel, thereby only completing the z -direction one step at a time. The drawback of these focus-search-methods is that the lateral resolution is limited to the pixels of the CCD sensor. Furthermore, the sharpness is obtained by evaluating multiple pixels (for example 8×8), so that the lateral resolution is again reduced by that factor.

Optical running time

These systems exploit the finite velocity of light. A short flash is emitted towards the object and the time is measured until the reflection reached the sensor. The durations are extremely short (approx. 0.3 ps for 0.1 mm) so the electronics must be very elaborate. One must bear in mind, that the information within any electrical circuit also travels with the speed of light. In contrast to other optical principles, the accuracy of running-time-measurements does not depend on the distance to the object.

Optical triangulation

Triangulation is the most commonly used optical measurement technology. It is very robust, cheap and easy to employ. Interferometry has been employed successfully for measuring distances in the range of 10^{-6} m to 10^{19} m , see [89]. The basic principle is

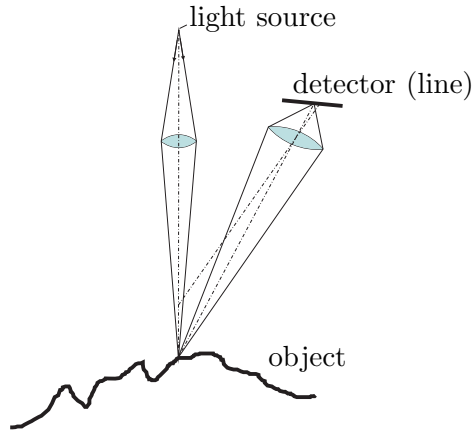


Figure 2: The basic principle of optical triangulation. The location of the maximum light amplitude on the detector is correlated to the distance of the object.

that a small light spot is projected onto the surface and observed from a fixed angle. The reflection from the spot is directed onto a CCD line detector or a similar system. This principle can easily be scaled to fit many applications. It requires at least some diffuse reflection from the surface and cannot handle slopes on the surface that are higher than the angle between emitted and detected beam. The triangulation can easily be extended to a line-scanning system by projecting a thin laser line onto the surface, which is then reflected onto a CCD matrix instead of a line sensor.

2.2 Fractal roughness - a generalized model

A very simple and convincing model to describe the roughness of a surface on multiple length scales is the fractal description. In the past, it has been analyzed by many researchers, also in the frame of theoretical contact mechanics [37][57][54][14]. The basic idea is to give a specific power-law correlation between different scale amplitudes. The *randomness* of different realizations is found in the phases. A surface z having such a characteristic behavior will be self-affine. It will have a certain appearance and a magnification z' of it at any spot will exhibit a very similar appearance and indeed 'look the same'. It is acceptable for the magnification in the vertical axis to be different from the lateral magnification:

$$z' = \lambda^H z(x/\lambda, y/\lambda). \quad (2.1)$$

In this equation H is the Hurst exponent which is of great importance in the current work. All these surfaces are called *self-affine*, or *self-similar* in the case of $H = 1$. In

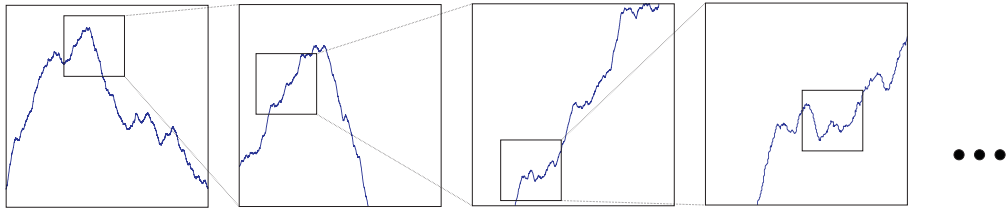


Figure 3: The fractal property. A magnification of the surface will 'look' like its parent. In this particular case $H = 1$, so the magnification parallel to the surface is equal to that perpendicular to it. Therefore every small square is magnified to give a larger square, whereas for $H < 1$ the square would have to be magnified as a high rectangle. In this figure only a cut through the surface is shown for clarity instead of the 3D shape.

many cases the fractal model is adequate from the macroscale [19] down to the lattice arrangement [6].

In the range of $H = 0 \dots 1$, a fractal dimension D_f can be associated to the surface, instead of the Hurst exponent H . The two quantities are related as follows [57]:

$$H = 3 - D_f. \quad (2.2)$$

In the past, many investigations about self-affine or self-similar surface only covered this range, but we will see that the equation governing the multiscale behavior does not naturally impose such a restriction. Indeed, the power spectrum $C_{2D}(|\mathbf{q}|) = C(q)$ of an isotropic fractal rough surface can be expressed as a power law. In [57] a clear derivation of the general form is given. I will follow the nomenclature given there by assigning bold letters to vectors:

$$C_{2D}(|\mathbf{q}|) = \frac{1}{(2\pi)^2} \int \langle h(\mathbf{x}) h(\mathbf{0}) \rangle e^{-i\mathbf{q} \cdot \mathbf{x}} d^2x. \quad (2.3)$$

Here $\langle \dots \rangle$ means ensemble averaging, i.e. averaging over a collection of different surfaces that have identical statistical properties. h is measured from the average surface plane, such that $\langle h \rangle = 0$. We write $\mathbf{x} = \frac{\mathbf{x}'}{\lambda}$ and obtain

$$C_{2D}(q) = \frac{1}{(2\pi)^2} \int \langle h(\mathbf{x}'/\lambda) h(\mathbf{0}) \rangle e^{-i\mathbf{q} \cdot \mathbf{x}'/\lambda} \lambda^{-2} d^2x'. \quad (2.4)$$

for a self-affine surface

$$\langle \lambda^H h(\mathbf{x}'/\lambda) \lambda^H h(\mathbf{0}) \rangle = \langle h(\mathbf{x}') h(\mathbf{0}) \rangle, \quad (2.5)$$

so we obtain

$$C_{2D}(q) = \frac{1}{(2\pi)^2} \int \langle h(\mathbf{x}') h(\mathbf{0}) \rangle e^{-i\mathbf{q} \cdot \mathbf{x}' / \lambda} \lambda^{-2-2H} d^2 x'. \quad (2.6)$$

We choose $\lambda = q$ and $\hat{\mathbf{q}} = \mathbf{q}/q$ and get

$$C_{2D}(q) = q^{-2(H+1)} \frac{1}{(2\pi)^2} \int \langle h(\mathbf{x}') h(\mathbf{0}) \rangle e^{-i\hat{\mathbf{q}} \cdot \mathbf{x}'} d^2 x'. \quad (2.7)$$

So the power spectrum decreases as

$$C_{2D} \propto q^{-2(H+1)} \quad (2.8)$$

with increasing wave number $q = |\mathbf{q}|$. Reasonable values for H in eq. 2.8 include $H \geq -1$ and we will see later that only for $H \geq 2$ will there be no more significant influence of H on the contact behavior.

The proof for linking H and D_f in eq. 2.2 is straight forward and can again be found in [57]. I will reproduce it here with only minor changes.

The fractal dimension tells us how many cubes with lateral size Δ are necessary to completely cover the surface.

$$N(\Delta) \propto \Delta^{-D_f} \quad (2.9)$$

for $\Delta \rightarrow 0$. Of course, covering a flat surface will require $(\frac{L}{\Delta})^2$ cubes, so the fractal dimension cannot be below 2. In any subdomain $\Delta \times \Delta$, the z-coordinate will cover a range of values Z_Δ that is proportional to Δ^H . More precisely, the range Z_Δ can be expressed in terms of the range of values covered in the overall domain $Z_\Delta = Z_L (\Delta/L)^H$, due to the self-affine property. As $H < 1$ we will obtain $Z_\Delta > \Delta$ for decreasing Δ . Any $\Delta \times \Delta$ subdomain will thus require $Z_L \frac{(\Delta/L)^H}{\Delta} \propto \Delta^{H-1}$ cubes, so filling up all the $L \times L$ domain will take a number of cubes proportional to $\Delta^{-(3-H)}$, so eq. 2.2 is valid.

2.3 Numerical surface generation

In sec. 2.2 it was claimed that the fractal model can accurately describe the surface roughness of many practically relevant cases, like surfaces resulting from fracturing. Still, if one wishes to investigate the properties of such fractal rough surfaces in more detail, it is necessary to generate the same with some repeatability for the following reasons

- fractal rough surfaces are *randomly* rough, so in order to extract a general behavior,

some averaging must be done over a multitude of surface samples. These samples must have the same power spectrum but they differ in the random phases.

- The exact decay of the power spectrum can be defined when using artificially generated samples. This is especially useful for probing different values of the Hurst exponent H .
- Using numerical approaches, we are able to generate surfaces that follow the fractal power law on as many scales as we wish, while real measured surfaces may be restricted in their fractal behavior due to the nature of the roughness or the measurement technology.

So even though we take a step away from the cases appearing in the real world, these idealized samples will facilitate to gain insights about the contact behavior of fractal rough surfaces. In the following subsection we will take a closer look at two widely used procedures that can effectively generate numerical samples of such idealized fractal rough surfaces.

2.3.1 Random Midpoint Algorithm (RMA)

The Random Midpoint Algorithm is a very simple and comprehensive way of generating fractal rough surfaces. It generates the surface features similarly to the way we imagine them. Because of its simplicity both in the implementation and the computational cost, it has been widely used in science as well as in computer graphics, for example in order to generate mountains in a computer game. The advantage of the RMA in computer graphics is the fact that one can obtain a coarse shape really quickly and effortlessly and refine it locally as the camera moves closer to a specific local spot.

1D line generation

Let us first look at the basic principle in one dimension, the generation of a fractal rough line. We start with a horizontal straight line. From here all we have to do is

- find the midpoint of the current line segment
- displace it up or down by a random amount within $\pm d$
- apply this algorithm to both of the resulting segments recursively, but restricting the maximum displacement in the substep to $\pm d_{sub} = d \cdot 2^{-H}$.

The result from multiple recursive steps (a – d) are shown in Fig. 4.

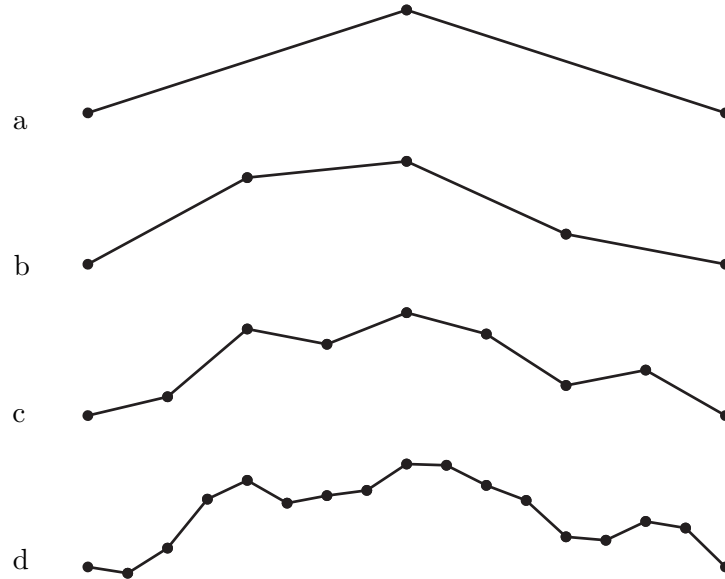


Figure 4: Explanation of the one dimensional random midpoint algorithm. Every recursive step alters the height information in the middle of the segment created by the previous step. Different values of H are obtained by limiting the amount of displacement in the recursive steps.

2D surface generation

Applying the RMA to a 2 dimensional plane again requires for the domain to be subdivided into smaller areas [44]. This time, two displacements are necessary per level. Refer to fig. 5 for the understanding of the following steps. We start with an initial square domain and then apply the following steps:

- Find the midpoint (large red dot) of the current square (black) and set its height to the average of the 4 corners plus a random displacement.
- Find the midpoint (small blue dot) of the center, two corners and the adjacent center that form a diamond (light blue). Set that midpoint to the average of its corners plus a random displacement.
- the midpoints of the last step form a square (light green) which is subject to the the algorithm to be applied recursively, again restricting the displacement in the substep to $\pm d_{sub} = d \cdot 2^{-H}$.

The RMA can easily be applied to grid sizes of $2^n + 1$ points in both the one dimensional and two dimensional case. The main drawback of this algorithm is the fact that the

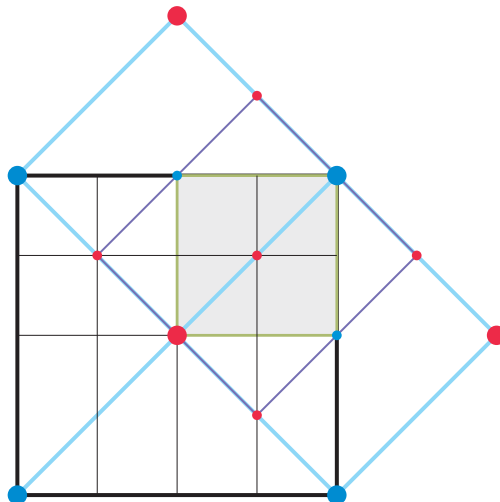


Figure 5: Explanation of the two dimensional random midpoint algorithm.

appearance of the resulting surface is determined by the first few random numbers. For that reason, the lower frequency amplitudes are subject to great scattering.

2.3.2 Inverse Fourier Transform (IFT)

For the numerical studies of the current work, all surfaces in both 1D and 2D were generated using the inverse fast Fourier transform. We wish for the numerical surface to satisfy the following properties

- the power spectrum goes according to eq. 2.8
- the phases are not correlated (random)

So in order to retrace the imagined fourier transform, we start from a desired power spectrum and impose a random phase distribution. Then we apply the inverse Fourier transform and end up with a surface that has the exact properties we desired.

1D line generation

The generation of a rough line via the inverse FFT starts from C_{1D} . The power-spectrum in the case of self-affine roughness can be derived in the very same way it is done for the 2D case in chapter 2.2. For a rough line, it is given by

$$C_{1D}(q) = const \cdot \left(\frac{q}{q_0}\right)^{-2H-1}. \quad (2.10)$$

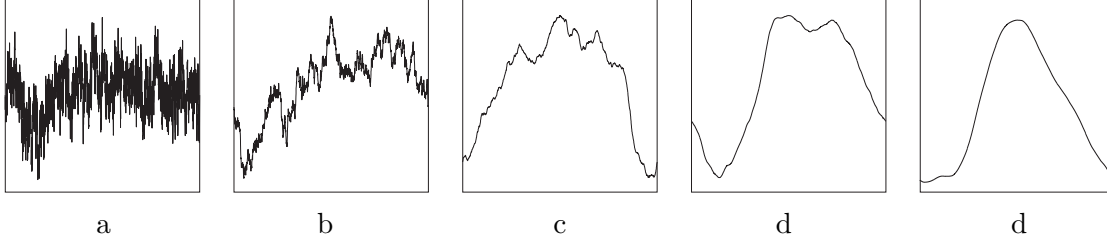


Figure 6: numerically generated line samples with different Hurst exponents: $H = 0$ (a), $H = 0.5$ (b), $H = 1.0$ (c), $H = 1.5$ (d), $H = 2.0$ (e)

The amplitudes are given by

$$B_{1D}(q) = \sqrt{\frac{2\pi}{L} C_{1D}(q)} = B_{1D}(-q). \quad (2.11)$$

The actual surface topography can then be obtained by evaluating

$$h(x) = \sum_{j=1}^N B_{1D}(q) \exp \left[i \left(\varphi - \frac{2\pi}{N} (j-1) \right) \right]. \quad (2.12)$$

See fig. 6 for examples of lines generated in this way.

2D surface generation

As we have seen in sec. 2.2, the power-spectrum of a self-similar surface with Hurst exponent H must read:

$$C_{2D}(q) = \text{const} \cdot \left(\frac{q}{q_0} \right)^{-2(H+1)}. \quad (2.13)$$

Because we are dealing with isotropic surfaces, the power spectrum only depends on the length of the wave vector \bar{q} , not on its orientation. For the amplitudes $B_{2D}(\bar{q})$ we can write

$$B_{2D}(\bar{q}) = \frac{2\pi}{L} \sqrt{C_{2D}(\bar{q})} = B_{2D}(-\bar{q}). \quad (2.14)$$

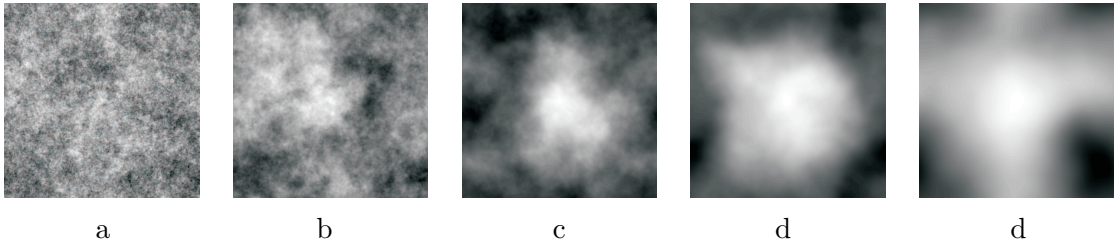


Figure 7: numerically generated surface samples with different Hurst exponents: $H = 0$ (a), $H = 0.5$ (b), $H = 1.0$ (c), $H = 1.5$ (d), $H = 2.0$ (e)

This choice ensures we only obtain real height values when synthesizing the surface topography as

$$h(\vec{x}) = \int_{q_{\min}}^{q_{\max}} dq B_{2D}(\vec{q}) \cos(\vec{q}\vec{x} + \varphi(\vec{q})). \quad (2.15)$$

The inverse fourier transform can effectively generate surfaces that obey the fractal power-law in a strict way. The resulting surfaces can be extended continuously by stitching the identical surface or line to its boundary.

The *fast* Fourier transform (FFT) is a widely spread algorithm that greatly reduces the computational costs of the evaluation of eq. 2.15 with grid sizes that are either powers of 2 or only have small prime factors.

3 Contact models

The urge to find general models to describe the contact of two rough bodies came up in the 1950s after Bowden and Tabor had pointed out the importance of the surface roughness. At this point, there were already analytical solutions available for the indentation of a single spherical indenter [31], of a flat punch [70] and later of an arbitrarily shaped radial symmetric indenter [20][77][78].

What was missing was a model that could successfully describe the contact of *nominally flat* surfaces. [2] Two different classes of approximative approaches for this problem can be identified:

- theories based on many distant discrete contact spots in the limit of low normal forces
- theories based on the assumption of having complete contact everywhere inside the apparent area of contact and then excluding subdomains with positive gap width.

The former line of theory was initiated by Greenwood and Williamson [25], while the later approach has been developed in the first years of the 21th century, mainly by Bo Persson. Only the elastic contact is considered here, so contact models with plasticity are not included. See [92] for a more extensive comparison.

The present work lays a theoretical foundation for fractal rough surfaces. It is my understanding that a surface may only be called fractal, if it does not have a characteristic wavelength. Of course, when investigating a nominally flat surface, the longest wavelength still having a considerable amplitude is somewhat characteristic. So the concepts introduced later in 4.4.1 and following cannot be applied directly to the *nominally flat* surfaces, but instead must be seen as an extension to the basic works of single indenter shapes. Nevertheless chapter 4.5.3 will show that a valuable insight can be gained in the area of nominally flat surfaces as well.

Let us now have a closer look at the two most commonly used classes of contact models.

3.1 Greenwood and Williamson

The basic observation that leads to the development of multi-asperity-models is that when two non-complying, solid surfaces come into contact, then in many cases true contact only occurs in a very small fraction of the apparent contact area. Possibly less than 1% of the surface area will be concerned. Furthermore, these areas of contact only arise in the vicinity of the highest roughness peaks, the asperities. When brought into

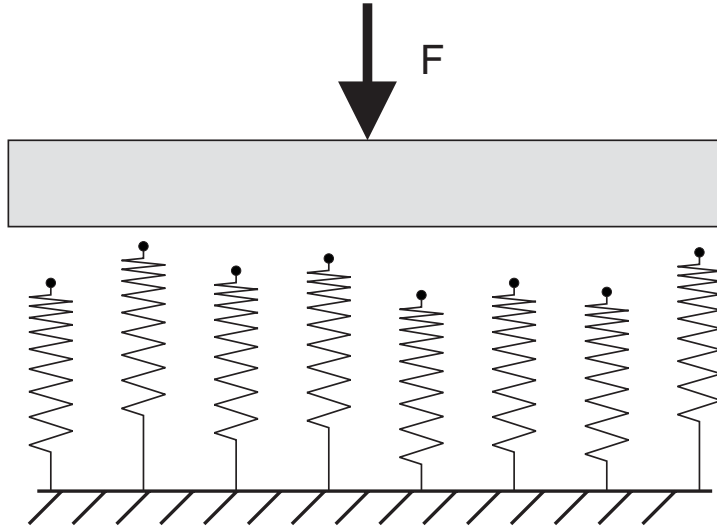


Figure 8: Basic explanation for multi-asperity models. The elastic rough surface is replaced by a large set of independent, nonlinear springs with a given height distribution. When the upper plane is lowered, more and more of these springs come into contact and add up to the overall contact force and stiffness. This model must not be confused with the MDR.

contact, these asperities will deform and there will be some elastic coupling between them. As long as the asperities are far enough apart, this coupling can be neglected [12], [11]. In the basic case of the GW-model, all asperities are assumed to behave in a Hertzian fashion and to have the same radius of curvature. Their heights are distributed in some random way – in the most basic case we will assume an exponential distribution

$$\varphi(z) = \begin{cases} \lambda e^{-\lambda z}, & z > 0 \\ 0, & \text{else} \end{cases}. \quad (3.1)$$

At this point, the model can be represented by a set of independent, nonlinear springs, that may or may not be in contact when the opposite plane is approached, see fig. 8 .

The analysis of this model is straightforward. Consider that every spring behaves in the same fashion. The normal force necessary to compress an asperity by distance d is assumed to follow

$$F_i(d) = c \cdot H_v(d) (d)^\beta, \quad (3.2)$$

where H_v is the Heaviside function to account for the fact that every spring can only apply a positive forces once it is contacted; c is a constant. We will now express the

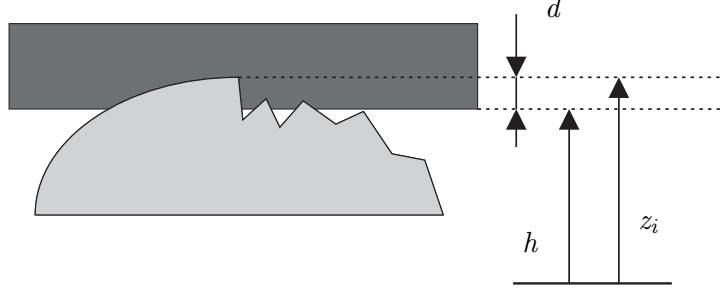


Figure 9: Coordinates used in the analysis of the multiasperity model. The lower grey area represents a single asperity with arbitrary shape, whose indentation behavior is given by eq. 3.2. The local indentation depth d can be obtained from the asperity maximum z_i and the position of the indenting plane h .

total normal force as a function of the position of the rigid opposite plate. For a given position, one has to sum up all the single asperity forces, that result from the local indentation with the help of eq. 3.2

$$F_N(h) = \sum_{i=1}^{N_0} F_i(d_i), \quad (3.3)$$

where $d_i = z_i - h$. See fig. 9 for coordinates used. With large N_0 we can use the probability distribution and integrate instead of summing over springs. We only account for the springs that are actually in contact, so we find:

$$F_N(h) = N_0 c \int_h^{\infty} \varphi(z) (z - h)^\beta dz \quad (3.4)$$

$$F_N = N_0 c \int_h^{\infty} \lambda e^{-\lambda z} (z - h)^\beta dz \quad (3.5)$$

$$F_N = \underbrace{N_0 c \lambda^{-\beta-1} \Gamma(1 + \beta)}_S e^{-\lambda h} dz \quad (3.6)$$

$$F_N = S e^{-\lambda h}. \quad (3.7)$$

The stiffness is given by the derivative of the force F_N with respect to d or $-h$:

$$k_N = \frac{\partial F_N}{\partial d} = -\frac{\partial F_N}{\partial h} = S \lambda e^{-\lambda h}. \quad (3.8)$$

Comparing eq. 3.7 and eq. 3.8 we finally find for the dependence of the normal contact stiffness as a function of the normal force:

$$k_N = \lambda F_N. \quad (3.9)$$

This relation is universally true for all nonlinear springs as defined in eq. 3.2 with $Real(\beta) > -1$. For example, it holds for the Hertzian contact ($\beta = 3/2$) with arbitrary radius of curvature. Other researchers have published works that are related to this model, the most important being the works by Bush, Gibson and Thomas [11], [12]. These investigations include different radii of curvature, Gaussian height distribution, non-symmetric asperities and other modifications. Ciavarella et.al [17] have improved the Greenwood Williamson model by including asperity interaction. They found linear dependence for the load-area-dependence. The contact conductance (and thus the stiffness) was and found close-to linear with a sub-linear behavior at intermediate, but not a distinct power law. An extensive comparison and analysis by Paggi and Barber of the models derived from GW can be found in [50]. For these models, a numerical analysis is carried out and the force-stiffness-relation is found to be a power-law

$$k_N \propto F_N^\alpha \quad (3.10)$$

with the power α between 0.8 and 0.9.

3.2 Persson

The contact theory of Bo Persson has a radically different approach than the multi-asperity theories. Instead of considering a multitude of independent asperities in the first step, this theory assumes full contact at the interface and determines the pressure probability distribution necessary to achieve this. Areas of non-contact are integrated using special boundary conditions. The basics of this model have been published in numerous papers [52],[53],[57],[54],[55] and have been compared to numerical results [14],[33],[41] with good agreement.

Let me redraw the basic idea of Persson on the dependence of the normal contact stiffness on the normal force. I will follow thoughts presented in [55]. We consider the contact of a flat elastic block and a stiff substrate which is randomly rough but nominally flat. The mean height of the substrate will be the origin of the z -coordinate. We denote the mean z -position of the deformed elastic block u which is also the mean separation. Let z_d be the coordinate of a distant point in the elastic block and p be the constant squeezing

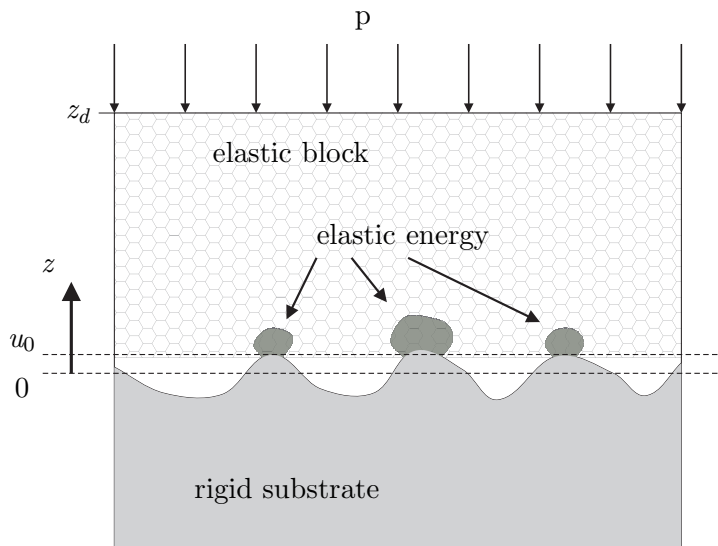


Figure 10: A flat elastic block in contact with a stiff substrate which is randomly rough, but nominally flat. The elastic energy will be located in the vicinity of the asperity contacts. Illustration reproduced from [55].

pressure. As the two bodies are pressed together, the mean separation will always be non-negative and become zero in the limiting case of full contact, so $u \geq 0$. We can thus express the pressure as a function of the mean separation:

$$p = p(u). \quad (3.11)$$

The elastic energy U_{el} stored in the substrate is located in the vicinity of the asperity contacts. It must be equal to the work done by the squeezing pressure

$$\int_u^\infty A_0 p(\tilde{u}) d\tilde{u} = U_{el}(u), \quad (3.12)$$

so that

$$p(u) = -\frac{1}{A_0} \frac{\partial U_{el}}{\partial u}. \quad (3.13)$$

Persson now states that with increasing pressure p , new asperity contacts form in such a way, that the size-distribution and pressure distribution always remain unchanged. More specifically, in [54], he states it can be derived from the the works of Bush, Gibson and Thomas [12] as a direct consequence of $A \propto F_N$. As the statistics of asperity contacts

remain the same, only their number grows. With the mean elastic energy and mean size per asperity being constant, both overall quantities grow in the same way

$$U_{el} \propto A. \quad (3.14)$$

From many works there is an almost universal agreement that the contact area rises linearly with the applied load, so we find a proportionality between squeezing force $A_0 p$ and the overall elastic energy

$$U_{el} = u_0 A_0 p(u), \quad (3.15)$$

where u_0 is a characteristic length that depends on the surface roughness and is of the order of the rms roughness [14]. We can thus express 3.13 as

$$p(u) = -u_0 \frac{\partial p}{\partial u}. \quad (3.16)$$

When defining the *interfacial* stiffness $K = A_0 \frac{\partial p}{\partial u}$, we find that it must rise linearly with the load $A_0 p$.

From my understanding eq. 3.12 and 3.13 are actually not correct. We can indeed derive U_{el} to find the force, but this has to be done with respect to the coordinate that refers to force location. In our case, this will be a distant point within the elastic body

$$A_0 p = -\frac{\partial U_{el}}{\partial z_d}. \quad (3.17)$$

For small forces, both eq. 3.13 and 3.17 coincide.

Characteristics of Persson's diffusion theory

In [53], Persson presents a theory for rubber friction which includes a theory of contact pressures, starting from full contact. This contact theory of Persson has been criticized by Manners and Greenwood [43], mainly because of the way this theory assumes full contact and later imposes contradicting boundary conditions to account for non-contacting areas. It can be expected that Persson's theory of contact can very effectively describe the contact mechanics in situations where the real contact area is comparable to the apparent area of contact.

In the past, Persson and co-workers have expressed their disagreement to the results presented in this work. In particular, they predicted the contact stiffness to always

rise linearly with the applied load, not in a power-law fashion. I wish to clarify some major differences that can shed some light onto to discrepancy between the different works. Together with the findings of chapter 4.5.3, these will help to understand, that the results presented here are not necessarily contradictory to the works of Persson. In contrast to this work, the theory of Persson considers:

- periodic boundary conditions, i.e. infinitely large bodies
- “fractal” rough surfaces, that include a roll-off or cut-off in the power-spectrum in the limits of long wavelengths, so effectively nominally flat surfaces
- contact configurations with a large number of contacts. It is said that these are necessary in order to get good statistics.
- the contact stiffness being the derivative of the normal force with respect to the *mean surface separation*, not to the approach of the two bodies.

As we have seen in this section, the last of the four differences should actually make both approaches more comparable in the low-load-regime, but the definitions certainly do not coincide for high forces.

4 Normal contact stiffness

Before discussing the contact stiffness in more detail, let me draw a clear picture of the problem in question. Subject of the investigation is the indentation of a rigid finite indenter into the elastic half-space, see fig. 11.

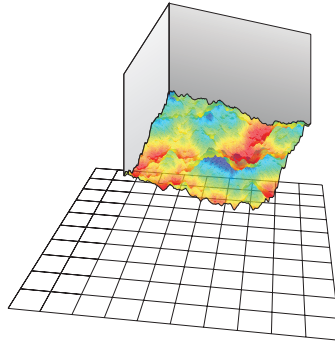


Figure 11: Schematic problem definition of the current work. A rigid squarish indenter with fractal surface topography is pressed into the elastic half-space.

Again, let me point out the particularities of this set-up compared to other research on the topic:

- The indenter has a finite square shape
- The surface outside the indenter is existing but left free to deform without pressure/load applied
- The size of the roughness features goes all the way up to the system size, it is not nominally flat. (see sections 5.1 and 3.2)

The fact that the global shape is a square actually doesn't play any role in the low-load-regime. Indeed, as long as the contact occurs only at some local spots, the elastic deformation of the half-space does not experience any influence from the rigid indenter edges, which are not in contact yet.

The contact stiffness will always be defined as

$$k = \frac{\partial F}{\partial d}, \quad (4.1)$$

where F is the normal force and d is the indentation depth of the rigid indenter with respect to the undeformed half-space surface. In other works, you may find the stiffness

being defined as the derivative of the normal force with respect to the *mean gap width* instead, see 3.2 and [1] [52] [32][33][41]. With our definition of k as the derivative of the normal force F with respect to the indentation depth d , it represents the resistance that the current contact configuration puts against the two bodies being approached any further. Given any contact configuration, the contact stiffness is the most interesting quantity to be determined, because it has exact proportionality to the electrical contact conductivity Λ_e

$$\frac{k}{E^*} = \Lambda_e \frac{(\rho_1 + \rho_2)}{2}. \quad (4.2)$$

E^* is the reduced elastic modulus calculated from the elastic moduli E and ν the Poisson's ratios of the two contacting bodies

$$E^* = \left(\frac{1 - \nu_1^2}{E_1} + \frac{1 - \nu_2^2}{E_2} \right)^{-1}, \quad (4.3)$$

ρ_1 and ρ_2 are the electrical resistivities [47] [26] [82] [5]. The heat conductivity Λ_t also has an exact analytical proportionality again only involving material parameters. With the specific thermal conductivity λ , the relation reads [4] [9] [70]:

$$\frac{k}{E^*} = \Lambda_t \frac{2}{(\lambda_1 + \lambda_2)}. \quad (4.4)$$

Note that in eq. 4.4 heat transfer via radiation or convective flow is neglected. A great amount of research has been conducted in the field of thermal conductivity, starting with the CMY-model [18] and subsequent works lead by Yovanovich. In [91], a review is given of the refinements and applications from 1963 – 2005. Furthermore it was shown that the normal contact stiffness k also correlates to the tangential contact stiffness k_t via the Mindlin-factor

$$\frac{k}{k_t} = \frac{2 - \nu}{2(1 - \nu)}. \quad (4.5)$$

This relation was originally found for circular contact spots [45] and was later confirmed numerically [14] for isotropic self-affine surfaces.

Using the relation from Lee and Radok [38][71], the contact stiffness of the elastic problem can also be transferred to give solution to the indentation of an indenter into a purely viscous medium. Indeed, the results of this current work and preceding papers [61], [63] have been applied successfully to this field of science [36].

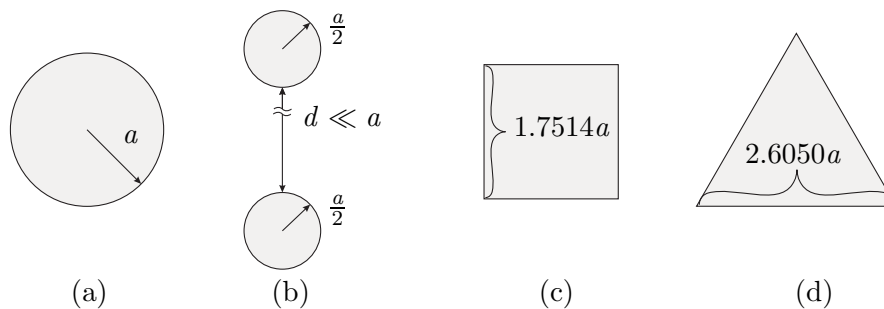


Figure 12: Different contact configurations leading to the same contact stiffness. All these 2D shapes can be associated with one particular 'contact length', that is the radius of an equivalent circular shape (a). Example (b) shows two distant circles which act in parallel. The dimensions of the square (c) and the triangle (d) are from [70].

4.1 Geometric properties of the contact stiffness

Consider two cases of rigid indenters being pushed into the elastic half-space. The first is a cylindrical shape with constant radius R and a flat bottom. The second case is the Hertzian sphere, pushed far enough, so that the contact area will be the exact same circle as in the first case. Both cases have been solved earlier, see [70]. Even though the pressure distribution inside the contact area is completely different and we did not even specify a normal force for the cylindrical indenter, the stiffness in both cases is the same and constant

$$\frac{k}{2E^*} = a. \tag{4.6}$$

Independently from the normal force or the pressure distribution inside the contact area, the contact stiffness maps the contact configuration (a circle) onto a length (its radius). This length can be called the Hertz-radius [31], the Holm-radius [83] or the contact length [70]. In fact it does not matter what indenter shape initially led to the circular contact region. Every time it is a circle, eq. 4.6 applies. For example, any rotational symmetric indenter shaped $z(r) = r^n$ will exhibit such behavior and also many superpositions, as long as the contact area does not develop into multiple rings [28]. Of course in real world applications the true contact area will not always be a plain circle, but for any finite contact configuration, an equivalent radius can be found.

The scaling of the contact stiffness has an interesting particularity. It scales linearly with the lateral extension, that is to say it does not scale linearly with the contact area, see fig. 13. When the contact stiffness for a given contact configuration is know, then stretching this configuration equally by λ in x and y will given the same contact stiffness multiplied

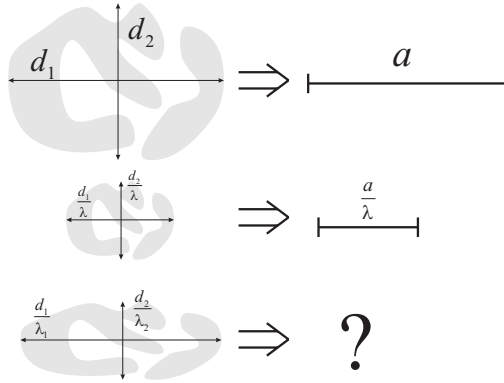


Figure 13: Scaling behavior of the corresponding contact stiffness for similar contact configurations. From the knowledge of the contact stiffness resulting from configuration (a), one can easily deduce that of configuration (b), but not in the case of configuration (c).

by λ . Stretching only one of the 2 planar extensions is not as trivial. This property of the contact stiffness to rise linearly with the system size is the key property that led to the development of the method of dimensionality reduction in contact mechanics. [70], [21], [28], [60], sec. A.2.

4.2 Dimensionless variables

The aim is to find the most general formulation for the dependence between normal force and normal contact stiffness. Therefore, an important step is to find dimensionless versions of both quantities that include as much information as possible about geometrical and mechanical observations that can be made independently from the particular surface type.

First, let us consider the normal contact stiffness. It has the dimension of force per length, N/m. From the considerations of the above section, we know that the contact stiffness scales linearly with the system size, measured in meters. A contact region that is within a square of length L cannot be associated with a stiffness that exceeds

$$k = 2E^*1.012L\pi^{-\frac{1}{2}}. \quad (4.7)$$

So different contact configuration become comparable if scaled to their maximum lateral extension L , see fig. 13. We conclude that the stiffness k must be normalized by L .

Furthermore it must always rise linearly with the reduced modulus of elasticity E^* . This

gives us the final dimensionless formulation \bar{k} of the contact stiffness k

$$\bar{k} = \frac{k}{E^*L}. \quad (4.8)$$

For the normal Force, a dimensionless formulation should be found as well. As per definition, the following is true:

$$F_N(d) = \int_0^d k(\tilde{d})d\tilde{d}. \quad (4.9)$$

Assuming the indentation d to start at the highest asperity peak. Now consider two surface topographies z_1 and z_2 with

$$z_1(x, y) = \lambda z_2(x, y). \quad (4.10)$$

When indenting these into the elastic half space, the very same contact configurations will be generated, thus the very same contact stiffness will be reached, only at different values of the indentation depth d :

$$k_1(d) = k_2(\lambda d). \quad (4.11)$$

So for the force of two rough surfaces to be equivalent, we have to use the normalization of the contact stiffness and a normalization to account the vertical extension of the roughness features. In the current work, this vertical extension is chosen to be the rms-roughness of the topography h

$$h = \sqrt{\frac{1}{L^2} \int_0^L \int_0^L [z(x, y)]^2 dx dy}. \quad (4.12)$$

We finally find for the dimensionless normal force

$$\bar{F} = \frac{F}{E^*hL}. \quad (4.13)$$

In [61] and [63], the same dimensionless quantities are motivated in a slightly different way.

4.3 Bounds on the assumptions

Whenever the contact stiffness is investigated in a finite system, say a square, some natural boundaries apply. The upper boundary is reached, when all discrete point have come into contact. In other words, when 100% of the apparent contact area is actually in intimate material contact and no gap exists between the bodies. The contact stiffness will simply be the value corresponding to the macroscopic indenter shape. In the case of a square, this limiting of the contact stiffness can be found in [70]

$$k = 2E^*1.012L\pi^{-\frac{1}{2}}, \quad (4.14)$$

wherein L is the length of one edge of the square.

Very similarly, a lower boundary exists in numerical investigations, that is closely related to the spatial resolution, the grid size. When only one single discrete grid point (x_a, y_a) is in contact, then the indentation depth d is equal to the deflection of the particular point a

$$d = u_a = \frac{1}{\pi E^*} \Delta K_{ijij} p_a. \quad (4.15)$$

Here $K_{ijij} = K_{00} \approx 3.5255$ (see 4.5.1) is the deflection caused by square unity pressure to its own local spot. As the normal force is $F_n = \sum p \Delta^2$ in the discrete system, we obtain for the contact stiffness

$$k = \frac{\partial F_n}{\partial d} = \frac{\Delta \pi E^*}{K_{00}}. \quad (4.16)$$

This value differs from the stiffness of a square indenter (eq. 4.14) by factor 0.78. The reason is that here we do not consider a rigid square with edge length $L = \Delta$ which would give us a pressure distribution with singularities near the corners. Instead we consider a homogenous pressure distribution and take a closer look at the deflection in the center. Instead of imposing a constant deflection, we keep the pressure distribution uniform.

So, whenever one single discrete grid point is in contact, the stiffness is constant as a numerical artifact. This must be kept in mind when evaluating numerical results. Also it is very clear that the finite resolution of the roughness effectively cuts off any roughness

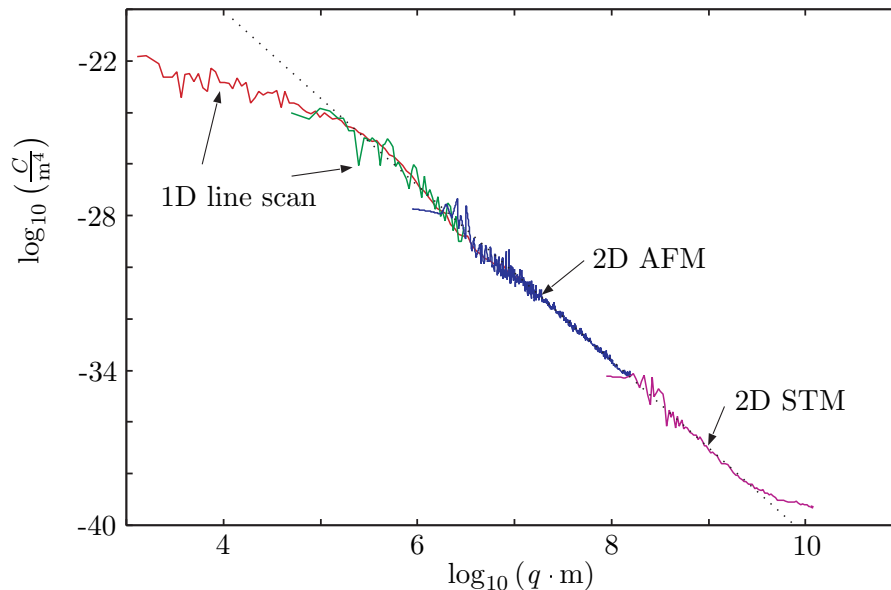


Figure 14: measured surface spectrum for a plate of grinded steel using mechanical line scanning, atomic force microscopy (AFM) and Scanning Tunneling Microscopy (STM). The rms roughness was $h = 0.5\mu\text{m}$. The dotted line corresponds to $H = 0.68$. Courtesy of Bo Persson [56].

features shorter than the grid space, so any behavior stemming from that range of the roughness is filtered out. In my experience, it is sufficient to discard any stiffness value below 20 times the limiting value eq. 4.16.

In addition to the geometrical or numerical boundaries mentioned, it is sensible to discuss the validity of the assumption from a physical point of view.

The first question to be answered is that of the geometrical model of fractal roughness. As we employ the fractal property eq. 2.1 in order to derive mechanical dependencies over multiple length scales, we must ensure that this assumption is correct in the first place.

Indeed it has been found in [19] and [3] that the fractal description holds for many different technical surfaces in the short-wave-range, with the Hurst exponent typically in the region of $0.6 < H < 0.9$. By combining multiple measurement techniques, Persson has shown for a specific sample [56], that the power-law of the surface spectrum eq. 2.8 is valid all the way to the atomic scale, see fig. 14.

If the surface roughness obeys the fractal law for even the smallest scales, then of course in the limit of small forces, continuum mechanics will fail rather than the fractal surface

description.

Among the assumptions in sec. 1 there is the approximation of the elastic half-space. We assume low slopes and a perfectly elastic behavior of the materials. This assumption is in fact not justified. Greenwood and Williamson introduced the plasticity index

$$\Psi = \frac{E^* \nabla z}{\sigma_0}, \quad (4.17)$$

where σ_0 is the hardness of the material. They argued that elastic contact can only occur for $\Psi < 2/3$. Note that the plasticity index does not depend on the normal force. For self-affine surfaces, the rms slope ∇z is given by

$$\langle \nabla z^2 \rangle \propto \int_{q_{\min}}^{q_{\max}} q^{-2H-2} q^3 dq, \quad (4.18)$$

with q_{\min} and q_{\max} being the minimum and maximum wave vector to occur on the surface. For $H < 1$ the integral diverges at the upper limit. We have seen that the fractal description is valid all the way down to the lattice scale, which effectively means there is no natural geometrical restriction to q_{\max} in the range of validity of continuum mechanics. In other words, for $H < 1$ fractal surfaces will always be in the plastic state when in contact.

Still, the assumption of elasticity on all scales does not play a crucial role in the current findings. The reason is that the contact stress at any particular scale has the order of magnitude

$$\sigma \approx \frac{E^* \nabla z}{2}, \quad (4.19)$$

where ∇z is the rms surface gradient corresponding to this scale [33]. The breakdown of the elastic behavior therefore occurs at the smallest scales corresponding to the largest rms surface gradient. The contact stiffness on the contrary is determined by the largest wavelength in the power spectrum of the surface roughness and is not sensitive to the occurrence on the atomic scale.

4.4 Analytical estimation

In the following section, I wish to give an analytical estimation for the dependence of the contact stiffness on the normal force for the scenario described in sec. 4. In 4.4.1, I will present the basic idea of how to find such a relation, which can be applied in both

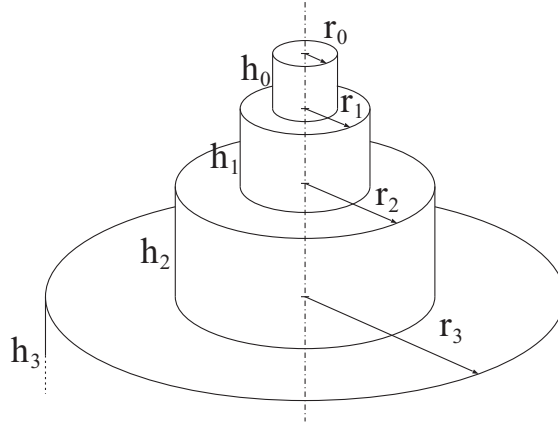


Figure 15: Very simple surface model satisfying the fractal law. The parameters of eq. 4.20 and eq. 4.21 in this example are $C = 2$, $H = 0.5$.

1D and 3D. This principle will be applied to randomly rough surfaces in 4.4.2. Also an alternate derivation in the frame of the MDR will be given, which helps to clarify the bounds of validity.

4.4.1 Power-Law dependence in a simple fractal model

Consider a rotationally symmetric elastic body that consists of multiple cylinders, see fig. 15. The dimensions of the cylinders starting with highest cylinder ($n = 0$) are defined

$$r_n = r_0 \cdot C^n, \tag{4.20}$$

$$h_n := h_0 \cdot C^{Hn}, \tag{4.21}$$

with $C > 1$ and $0 \leq H \leq 1$.

Let us now imagine the indentation process when this indenter is pressed against a rigid wall, see fig. 16.

The resulting contact areas are shown on the left hand side. Let us now assume that in each step, the contact stiffness is only determined by the largest radius in contact and proportional to the same. This is a reasonable assumption as can be found in the works of Holm [87]. Under this assumption, the stiffness as a function of the applied force will consist of multiple, discrete steps, see fig. 17. For the dark spots marked in this figure, the contact stiffness being proportional to the current radius is

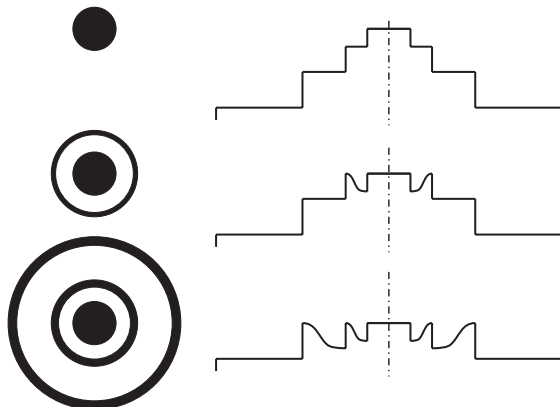


Figure 16: Indentation steps of the elastic indenter. The deformations are not scaled correctly. On the left hand side one can see qualitatively the resulting real area of contact corresponding to the deformed state displayed on the right hand side.

$$k_n = E^* r_0 C^n. \quad (4.22)$$

The corresponding force at each spot consists mainly of the stiffness of the last cylinder times the height of this last cylinder, giving

$$F_n = k_n h_n = E^* r_0 C^n h_0 C^{Hn} = E^* r_0 h_0 C^{(H+1)n}. \quad (4.23)$$

We can now eliminate C and obtain

$$k_n \propto F_n^{\frac{1}{1+H}}. \quad (4.24)$$

It shall be noted that the shape of the indenter shown in fig. 15 is actually very similar to a smooth indenter $z = r^H$. For this smooth indenter, the contact problem has been solved earlier by Galin and Sneddon [20],[78],[23] who equally found eq. 4.24. Also this indenter shape satisfies the self-affinity property eq. 2.1. The idea is developed further and employed in sec. 5.2.

We will see later that eq. 4.24 agrees well with the numerical results in the vicinity of $H = 1$ but not so much near $H = 0$. In the following section we will see why $H = 0$ is a natural boundary for its validity.

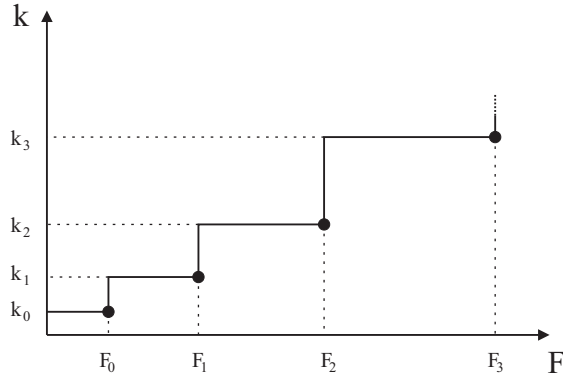


Figure 17: Schematic dependence of the contact stiffness on the applied load for the indenter model presented in fig. 15.

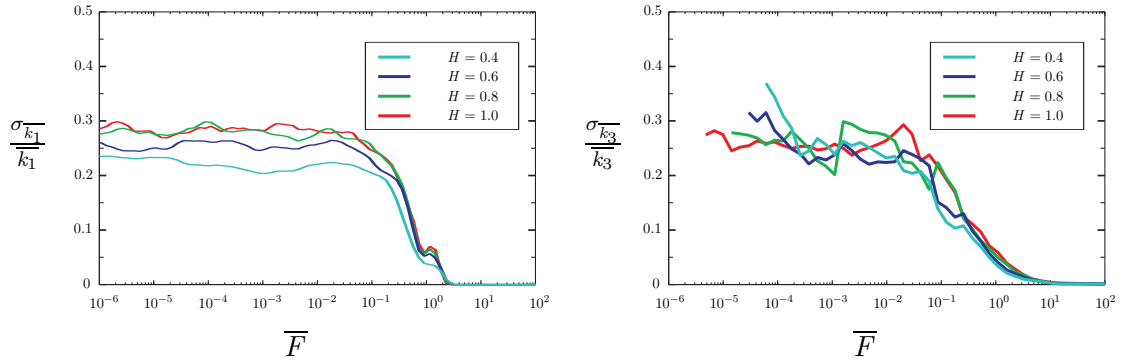


Figure 18: Standard deviation of the stiffness for different surface realizations of the same type as obtained by means of the 3D BEM (left) and the 1D MDR (right).

4.4.2 Implementation to random rough surfaces

I now want to show how to apply the above mentioned argument to fractal rough surfaces. Let us call fractal surfaces to be *of the same type* if they have the same Hurst-Exponent H , same reduced modulus of elasticity E^* , same rms roughness h , same system size L and only differ in the random phases that were used in order to generate them.

We can assume that surface of the same type have the same contact stiffness when loaded with the same normal force. Indeed my numerical studies sec. 4.5.1 and sec. 4.5.2 show that the standard deviation of the stiffness for different samples is limited to about 30% over many orders of magnitude for the normal force F , see fig. 18.

So there is indeed an invariant characteristic stiffness value for surfaces *of the same type*. Furthermore when using the normalized definitions of contact stiffness (eq. 4.8) and normal force (eq. 4.13), then any inequality in E^* , L or h is already taken into account

and we only need to demand for the Hurst exponent to be identical.

Let us do a little gedankenexperiment. A rigid indenter defined on a square with system size L_1 is forced into the elastic half space. Then, a specific contact configuration arises, see fig. 19. It is only now that we learn that the indenter is in reality part of a larger indenter $L_2 = \lambda L_1$ which of course has the same Hurst exponent. Both the small indenter and the larger one are of the same type. As we did not alter any physical quantities during the revelation of the bigger system size, all *physical* quantities remain unchanged, that is to say, all quantities that still have dimensions. So we find

$$F_1 = F_2, \tag{4.25}$$

$$k_1 = k_2. \tag{4.26}$$

From $L_2 = \lambda L_1$ and eq. 2.1 we know that for the rms roughness of both we have

$$h_2 = \lambda^H h_1. \tag{4.27}$$

In terms of the dimensionless stiffness we can write:

$$\bar{k}_2 = \frac{k_1}{E^* L_2} = \frac{k_1}{E^* \lambda L_1} = \frac{\bar{k}_1}{\lambda} \tag{4.28}$$

and for the dimensionless normal force

$$\bar{F}_2 = \frac{F_1}{E^* L_2 h_2} = \frac{F_1}{E^* \lambda L_1 \lambda^H h_1} = \frac{\bar{F}_1}{\lambda^{H+1}}, \tag{4.29}$$

so that we finally find

$$\frac{\bar{k}}{\bar{k}'} = \left(\frac{\bar{F}}{\bar{F}'} \right)^{\frac{1}{H+1}} \tag{4.30}$$

and thus

$$\bar{k} \propto \bar{F}^{\frac{1}{H+1}}. \tag{4.31}$$

For fractal rough surfaces of the same type and the same Hurst exponent H .

V.L. Popov also found an alternate derivation of this behavior, which not only finds the same power-law behavior but also states its range of validity in terms of H . This is done by analyzing the height distribution of the self-affine roughness, adding modes one at a time. The analysis is done in the frame of the Method of Dimensionality Reduction

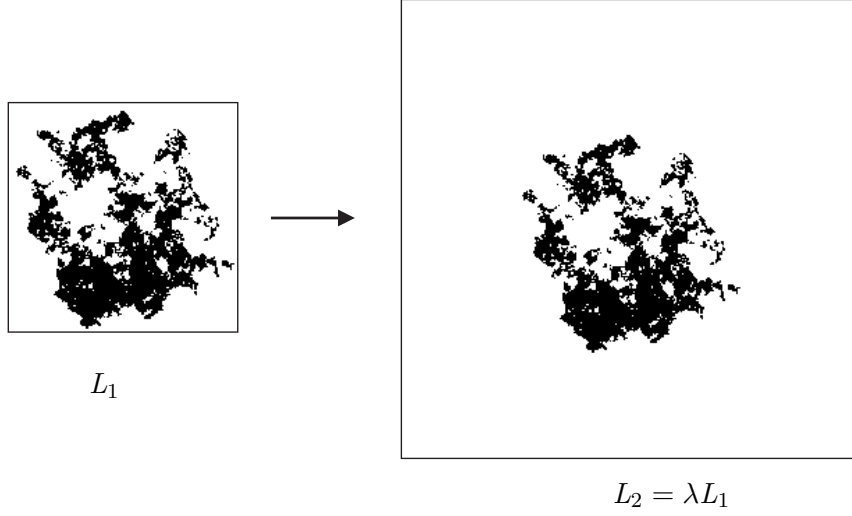


Figure 19: Gedankenexperiment for motivating the power-law. A contact configuration results from indenting a fractal rough indenter defined in square (1) into the elastic half-space. The very same configuration is obtained by indenting a larger fractal indenter (2) by the same indentation depth.

(MDR). Any reader that is new to the methodology of MDR is referred to sec. A.2 and the literature mentioned there.

Let us first consider a one-dimensional sine wave line of length L in its simplest form

$$z = h_0 \cos(qx), \quad (4.32)$$

which is brought into contact with a flat Winkler foundation, that has the stiffness per length E^* . The force F necessary to obtain the indentation depth d is given by

$$F(d) = \frac{2}{\pi} LE^* h_0 \left[\arcsin \left(\sqrt{\frac{d}{2h_0}} \right) - \sqrt{\frac{d}{2h_0}} \sqrt{1 - \frac{d}{2h_0}} \right]. \quad (4.33)$$

For small forces this can be approximated as

$$F(d) \approx \frac{2}{\pi} LE^* h_0 \frac{2}{3} \left(\frac{d}{2h_0} \right)^{3/2} = \frac{2^{1/2}}{\pi} LE^* h_0^{-1/2} d^{3/2}. \quad (4.34)$$

The waviness will be completely flattened out at

$$\widehat{F}(d = 2h_0) = LE^* h_0. \quad (4.35)$$

As a second step, let us now assume a superposition of two sine waves

$$z = h_1 \cos(q_1 x) + h_2 \cos(q_2 x). \quad (4.36)$$

Assuming for the frequencies to satisfy $q_2 \gg q_1$, we can define a local indentation of the longer wave

$$d(x) = d - h_1 \frac{(q_1 x)^2}{2}. \quad (4.37)$$

The force resulting from the indentation of a single long-wave maximum can be expressed by the integral

$$F = \int_{-\frac{1}{q_1} \sqrt{\frac{2d}{h_1}}}^{\frac{1}{q_1} \sqrt{\frac{2d}{h_1}}} \frac{2}{\pi} E^* h_2 \left[\arcsin \left(\sqrt{\frac{d(x)}{2h_2}} \right) - \sqrt{\frac{d(x)}{2h_2}} \sqrt{1 - \frac{d(x)}{2h_2}} \right] dx. \quad (4.38)$$

At $d = 2h_2$, the shorter wave is flattened out for the first time. The force \hat{F} necessary is

$$\hat{F} = \int_{-\frac{1}{q_1} \sqrt{\frac{4h_2}{h_1}}}^{\frac{1}{q_1} \sqrt{\frac{4h_2}{h_1}}} \frac{2}{\pi} E^* h_2 \left[\arcsin \sqrt{1 - \frac{h_1 (q_1 x)^2}{4h_2}} - \sqrt{1 - \frac{h_1 (q_1 x)^2}{4h_2}} \sqrt{\frac{h_1 (q_1 x)^2}{4h_2}} \right] dx. \quad (4.39)$$

Substitution of $x = \xi \frac{2}{q_1} \sqrt{\frac{h_2}{h_1}}$ leads to

$$\hat{F} = \frac{8}{\pi} E^* \frac{h_2^{3/2}}{q_1 h_1^{1/2}} \int_0^1 \left[\arcsin \left(\sqrt{1 - \xi^2} \right) - \sqrt{1 - \xi^2} \sqrt{\xi^2} \right] d\xi = \frac{16}{3\pi} E^* \frac{h_2^{3/2}}{q_1 h_1^{1/2}}. \quad (4.40)$$

The stiffness is proportional to the length in contact:

$$\hat{k} = E^* \frac{4}{q_1} \sqrt{\frac{h_2}{h_1}}. \quad (4.41)$$

For self-affine rough lines, the self-affinity property eq. 2.1 is valid. This means that if the rough line is composed as a sum of harmonics

$$z = \sum_{n=0}^N h_n \cos(q_n x) \quad (4.42)$$

with frequencies

$$q_n = q_0 C^n \quad (4.43)$$

then the amplitudes must read

$$h_n = h_0 C^{-nH}. \quad (4.44)$$

Here $C > 1$ is a magnification constant. We now want to analyze the profile for the specific case, where the roughness at one particular scale is completely flattened out before, on the previous (longer) scale, the adjacent maximum reaches contact. In the sample of fig. 20 this is obviously the case, see the indentation at the d_3 line. With these conditions, contact will regularly occur at one continuous spot. For every scale n , we can find \widehat{F} according to 4.40

$$\widehat{F}_n = \frac{16}{3\pi} E^* \frac{h_{n+1}^{3/2}}{q_n h_n^{1/2}}. \quad (4.45)$$

The corresponding stiffness reads

$$\widehat{k}_n = E^* \frac{4}{q_n} \sqrt{\frac{h_{n+1}}{h_n}}. \quad (4.46)$$

Inserting 4.43 and 4.44 leads to the dependency

$$k \propto F^{\frac{1}{H+1}}. \quad (4.47)$$

Let us now test the assumptions of the new derivation. For eq. 4.47 to be valid, we need to impose restrictions on the modes of different orders.

1. The amplitude of the $n + 1$ roughness must be smaller than that of the n -th order.
2. When indenting the roughness at one scale, there must be a subsequent roughness following in the same order of magnitude, or else the smaller scale roughness will be negligible.

The first statement requires $h_{n+1} < h_n$. From eq. 4.44 it is clear that this is the case for

$$H > 0. \quad (4.48)$$

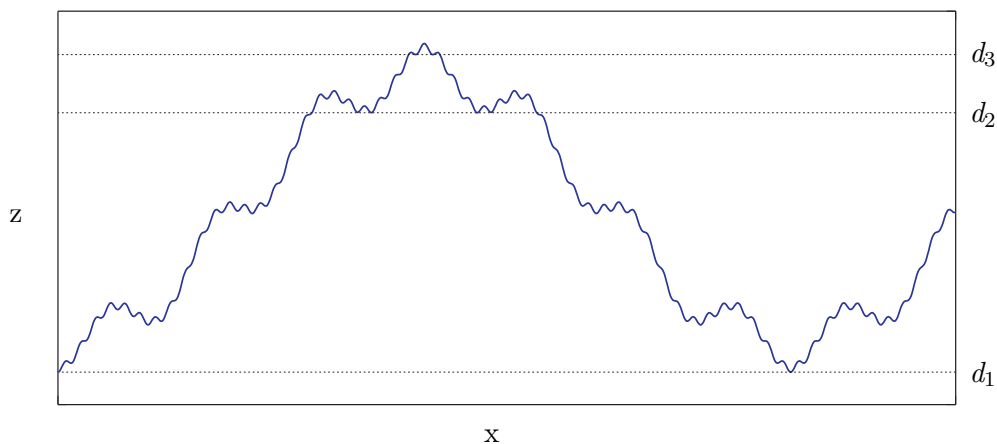


Figure 20: example of a rough line with 3 scales. $H = 0.9$, $C = 7$.

The second requirement is fulfilled approximately when

$$h_{n+1} > \frac{\lambda_{n+1}^2}{4\pi^2 R_n}. \quad (4.49)$$

Here $\lambda_n = \frac{2\pi}{q_n}$ is the wavelength of a mode and $R_n = h_n^{-1} q_n^{-2}$ is its radius of curvature near the maximum. Eq. 4.49 can also be expressed as

$$h_{n+1} q_{n+1}^2 > h_n q_n^2. \quad (4.50)$$

Inserting 4.43 and 4.44 leads to the requirement

$$H < 2. \quad (4.51)$$

So it can be seen that the power law can only be valid for

$$0 < H < 2, \quad (4.52)$$

but deviations are expected in the vicinity of these limits.

We have seen that simple analytical considerations suggest that for self-affine rough surfaces, there must be a power-law dependence between the normal contact stiffness and the normal force, in the form of eq. 4.31. This dependency is expected to be valid for rough surfaces with Hurst exponent in the range of $0 < H < 2$. Unfortunately, no expression for the prefactor in the power-law was derived, but it can still be found numerically as will be shown in the next section.

4.5 Simulation

In the frame of this work, extensive numerical studies have been conducted for a broad range of surfaces, having multiscale roughness. The surfaces were generated using the inverse Fourier transform, see sec. 2.3.2. Two fundamentally different methods were applied to this problem

- the 3D Boundary Element Method
- the 1D Method of Dimensionality Reduction

The former has been used in many previous investigations and is a widely accepted method in contact mechanics. The basic principles and optimization techniques can be found in A.1 and A.1.2. Even though a lot of time and knowledge was invested into these simulation routines, it still turned out to be a time-consuming process. The details of the numerical studies will be given below.

In contrast, the Method of Dimensionality Reduction is less known, but it has an incredible potential. Again, the numerical details of the method can be found in the appendix A.2. In the corresponding sections, the parameters and results of the numerical studies will be discussed.

4.5.1 3D Boundary Element Method (BEM)

The normal contact problem defined in sec. 4 has been treated numerically using the 3D-boundary element, as described in appendices A.1.1 and A.1.2. The first results of these simulations were published in [61]. At that point the interpretation was still weak, but the basic trends of dependencies were found already. In this paper and two following publications [63], [60] results were presented for grid sizes of 1025×1025 and later 2049×2049 points. Let's see the raw numerical results. Fig. 21 shows the averaging over multiple samples. The dimensionless quantities of force and stiffness are chosen according to eq. 4.13 and eq. 4.8.

One can easily see the saturation in the stiffness for high values of the normal force, as predicted in sec. 4.3, eq. 4.14. Furthermore the transition to a power-law-behavior for smaller forces is found. Note that these results only feature values of D_f from 2 to 3 (H from 1 to 0), following the arrow. In [61], an analysis of the dependency is given, with the exponent and prefactor of the resulting power-law read from the numerical data.

For the following more detailed analysis, a newer set of simulation data will be used. The main reasons for re-doing the already-published simulation results were to

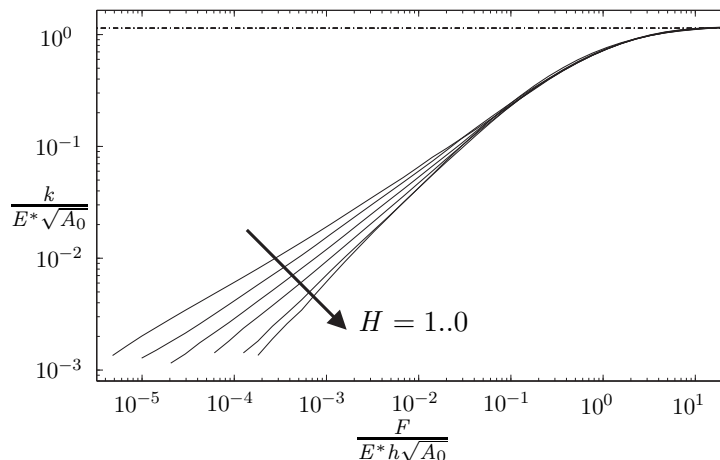


Figure 21: Dependency of the dimensionless normal contact stiffness as a function of the applied dimensionless normal force. Obtained by means of the 3D BEM.

- investigate more values of H
- take a closer look at the prefactor in the power-law.
- use a finer increment in the normal force

In all these simulations, the highest normal forces require the most calculation time, but here the stiffness is already saturated, so this region is of minor interest. For the following new calculations, forces were restricted to $\bar{F} = 0.07$ in terms of the dimensionless quantity defined in eq. 4.13. In the 3D case, surfaces were generated for the Hurst Exponent equally spaced by 0.15 from -0.5 to 2.95, 24 different values in total. For each one, 50 surfaces were evaluated to get an adequate averaging. 100 values for the force were used, spaced in a logarithmic fashion. Then, the power-law region was fitted to give

$$\bar{k} = \zeta \bar{F}^{\alpha(H)}. \quad (4.53)$$

The approximate results from the curve-fitting are found in sec. 4.5.3, fig. 27. and fig. 28.

4.5.2 Method of Dimensionality Reduction (MDR)

In this section we want to treat the application of the method of dimensionality reduction to the problem of fractal rough surfaces. Usually when it comes to reporting on numerical

studies, results are presented, based on some lengthy simulation runs, that were executed on specialized computer architectures using highly adapted code. Then, from these limited results, conclusions are drawn.

The neat thing about the method of reduction of dimensionality is that it requires neither complicated programming nor much computational time. In fact all of the results presented here can be reproduced by anyone who possesses basic programming skills within a couple of hours and programs will run seconds to minutes with any personal computer. Therefore it is no wonder that the results shown here display a greater range in parameters, greater number of samples to produce statistics and greater accuracy in terms of spatial resolution – it is all due to the extremely small complexity of the method.

The method itself is introduced briefly in appendix A.2. Furthermore, a great variety of publications exists, featuring the basics of the method [21], [22], [28], [40], extensions to more tribological phenomena [66] and applications, including dynamic problems [81]. Very recently, a book appeared in German including all state-of-the-art insights about the method [67]. The best current English summary is found in [65].

We start with surfaces generated in the way that was proposed by Geike in [21]:

$$C_{1D} = \pi q C_{2D}. \tag{4.54}$$

In the case of a fractal rough surface we have

$$C_{2D} = C_0 \cdot (Lq)^{-2(H+1)}, \tag{4.55}$$

$$C_{1D} = \pi C_0 \cdot (Lq)^{-2H-1}. \tag{4.56}$$

Interestingly, this choice also assures that the fractal property is conserved with the 1D rough line:

$$z' = \lambda^H z(x/\lambda, y/\lambda). \tag{4.57}$$

Indeed, the derivation provided in sec. 2.2 can be applied in the same way, only taking into account one spatial dimension instead of two.

We can now analyze these surfaces using the method of dimensionality reduction. See for example fig. 22. It was generated in 4 seconds and features 11 values of H , times 1500 surface samples of 500 grid points, times 400 force values.

Both saturation values for small and high forces can be seen directly. In the medium range, a power-law is observed. The exponent can be obtained by extracting the relevant

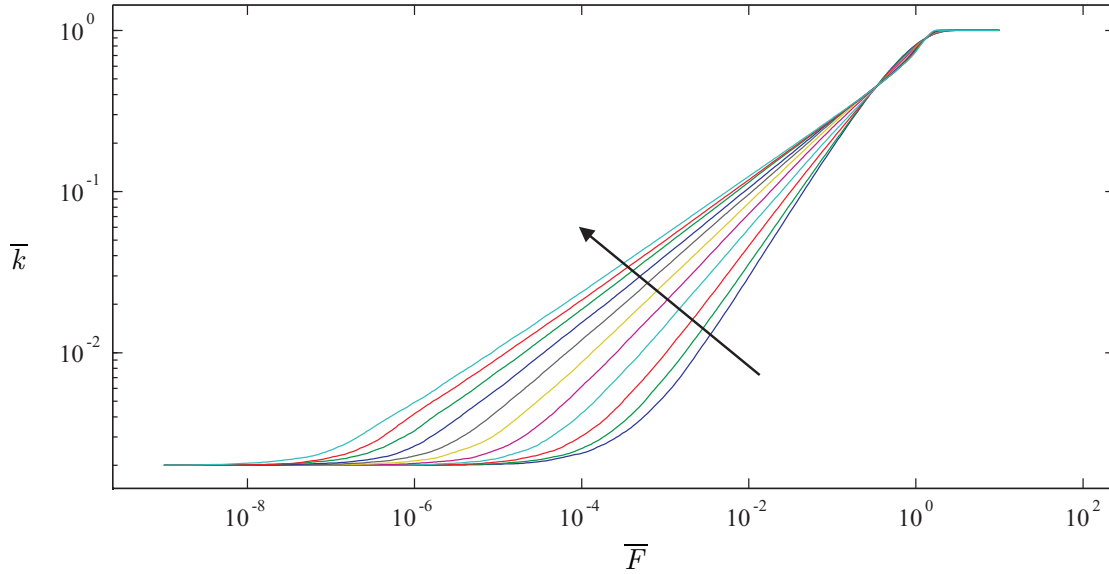


Figure 22: Numerically obtained dependency of the dimensionless normal contact stiffness as a function of the applied dimensionless load, using the MDR. H ranges from 0 to 2, following the arrow.

region of the curve and applying a curve fitting algorithm. In the current work, the parameters of a linear dependency were adjusted to best reproduce the dependency of the logarithm of stiffness vs. the logarithm of forces in order to account for all scales similarly. In fig. 22, H ranges from 0 to 2. We will call this region the Pohrt/Popov-range, because it limits the validity of the Pohrt/Popov-power-law eq. 4.53 with $\alpha = (H + 1)^{-1}$. Let us have a closer look at the slope of the curves in the power-law region.

We can see the basic run of the curve in fig. 23, starting from a constant value for $H < 0$, going through the Pohrt/Popov-region and ending at the Hertzian regime. What is interesting to see is that apparently the constant for low value of H depends on the systems spatial resolution. We can see this limiting value for system sizes $N = 2^9$ and $N = 2^{11}$ and observe that it depends on the resolution of the generated surface. More specifically for this region, the resulting power in the force-stiffness-relation depends on the number of modes that are included. With small H , even the shortest roughness features still have a considerable influence.

The dependency results in 1D from the height distribution in the following way. Assume the stiffness depends on the normal load as

$$\partial F / \partial d \propto F^\alpha. \quad (4.58)$$

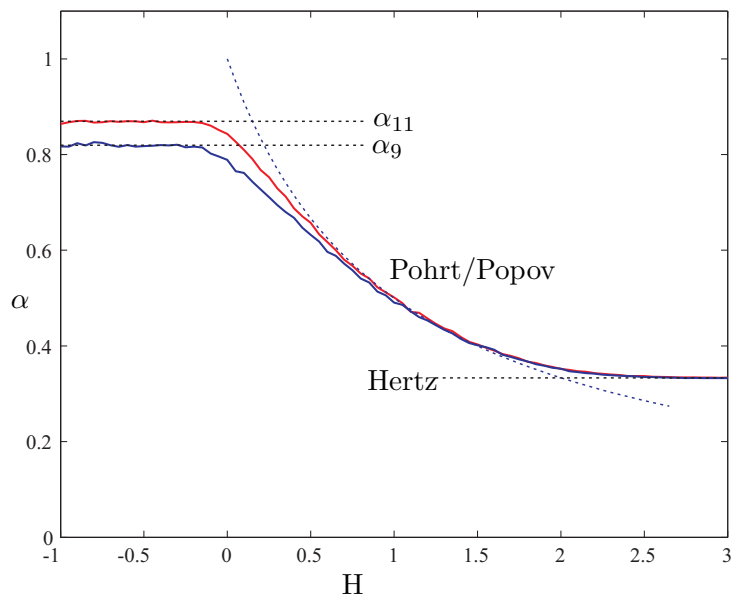


Figure 23: Numerically obtained dependency of α on H using the MDR. The green curve is for system size $N = 2^{11}$, the blue one for $N = 2^9$. The values have been obtained by finding best linear fits to the curves shown in fig. 22 .

With $\alpha < 1$, then there is an indentation depth where the normal force vanishes, the highest asperity. We call the indentation d starting from that point u . The probability density of heights $\Phi(z)$ also refers to this point. In the frame of the MDR, the normal force can be expressed as

$$F = A \int_0^u \Phi(z) (u - z) dz. \quad (4.59)$$

Assuming a power-law dependency $\Phi(z) \propto z^\beta$, we obtain

$$F \propto \int_0^u z^\beta (u - z) dz \propto u^{\beta+2}. \quad (4.60)$$

So the stiffness is proportional to

$$k = \partial F / \partial u \propto u^{\beta+1}, \quad (4.61)$$

$$k \propto F^{\frac{\beta+1}{\beta+2}}, \quad (4.62)$$

which gives us the correlation between powers α and β :

$$\alpha = \frac{\beta + 1}{\beta + 2}, \quad (4.63)$$

$$\beta = \frac{2\alpha - 1}{1 - \alpha}. \quad (4.64)$$

We will now show how to determine β from the number of modes of the rough line that is generated with the help of

$$z(x) = \sum_q B_{1D}(q) \exp(i(qx + \varphi(q))), \quad (4.65)$$

$$B_{1D}(q) = \sqrt{\frac{2\pi}{L} C_{1D}(q)} = B_{1D}(-q), \quad (4.66)$$

with random phases $\varphi(q) = -\varphi(-q)$ from $[0, 2\pi)$.

Eq. 4.65 is a sum of N harmonics with wave vectors ranging from q_{\min} to q_{\max} with the step size of $\frac{L}{\Delta x}$. We assume $N = 2^m$. Lets us first consider the case of a single harmonic, see fig. 24a. The resulting sine-function can be approximated in the vicinity of its maximum

$$z(x) \propto x^2, \quad (4.67)$$

which allows us to count the coordinates x and z in order to obtain the height distribution. The number of points in x in the interval dx equals $dN = dx/\Delta x$, while on the z -axis we have $dz = f'(x)dx = 2x dx$. The resulting height distribution reads

$$\Phi_1(z) = \frac{dN}{dz} = \frac{1}{\Delta x} \frac{1}{f'(x)} \propto x^{-1} \propto z^{-1/2}. \quad (4.68)$$

With two superposed sine wave of similar frequency, we obtain a beating wave (fig. 24b). Every maximum here adds to the height distribution as described by eq. 4.68. Yet the maximum itself consists of a series of parabolas. The overall height distribution can thus be calculated as

$$\Phi_2(z) \propto \int_0^z (z - z')^{-1/2} z'^{-1/2} dz' = \int_0^1 (1 - \xi)^{-1/2} \xi^{-1/2} d\xi = \pi, \quad (4.69)$$

resulting in a constant height density that does not depends on z . Similarly, four modes will generate a modulated beat wave (beat wave of the 2nd kind, see fig. 24c), with the

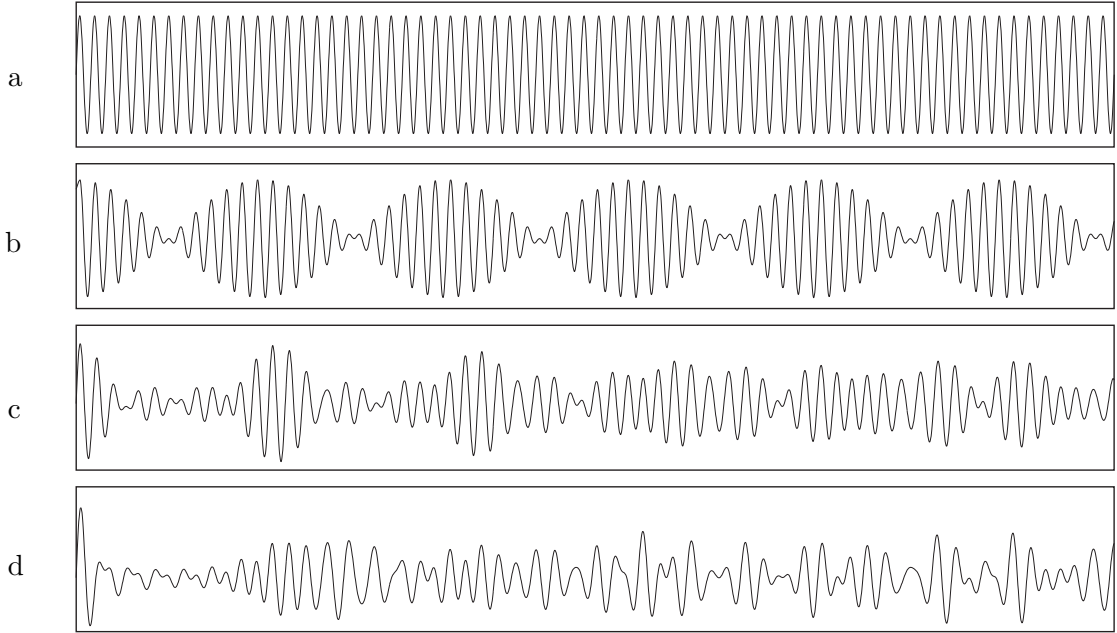


Figure 24: Superposed sine waves with similar frequency and amplitude. (a) one mode, (b) two modes, (c) four modes, (d) eight modes.

height distribution

$$\Phi_3(z) \propto \int_0^z \text{const} \cdot z'^{-1/2} dz' \propto z^{1/2}. \quad (4.70)$$

The sum of 8 modes leads to the beat wave of the 3rd kind.

Continuing from here, every next step leads of to a height distribution that can be calculated from the previous one, according to

$$\Phi_{n+1} = \int_0^z \Phi_n(z - z') z'^{-1/2} dz'. \quad (4.71)$$

Every integration increases the power by $1/2$. The power β resulting from N modes can thus be expressed as

$$\beta = -\frac{1}{2} + \frac{1}{2} \log_2(N), \quad (4.72)$$

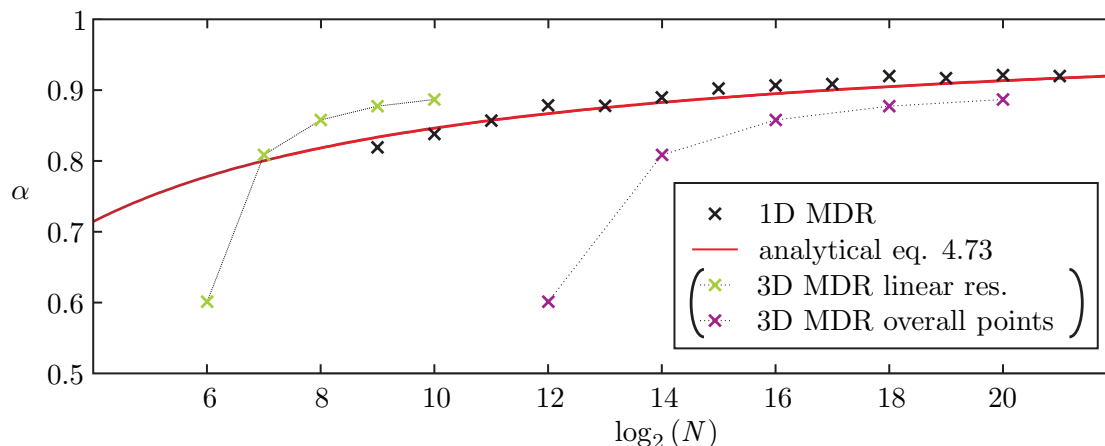


Figure 25: dependency of the exponent α for low H on the system size. Black crosses are obtained numerically using MRD, red line according to eq. 4.73. The colored crosses are identical results from a 3D BEM calculation, referring to the linear system size (green) or the overall grid points N^2 (purple).

so for the power α we finally get

$$\alpha = \frac{\beta + 1}{\beta + 2} = \frac{1 + \log_2(N)}{3 + \log_2(N)}. \quad (4.73)$$

For this result to be valid, the amplitudes of the summed waves must not differ too much, as can be seen from the 2nd step already; the beat wave's behavior near the maximum is not altered, when two sine wave are added with different but close amplitudes. Fig. 25 shows eq. 4.73 together with the numerically determined (MDR) exponents from the force-stiffness-relation. It can be concluded that the resolution has a major influence on the results of fractal rough surface simulations, especially in the case of low Hurst exponents or a considerable Cut-off (which corresponds to $H = -1$) [93].

A similar dependency can be found in 3 dimensions, see fig. 26 and the colored crosses of fig. 25. As I not have an analytical derivation for this resolution-dependency, N can be interpreted in two different ways in that plot.

4.5.3 Comparison numerical and analytical

At this point we have seen three totally different approaches to predict the dependency of k on F .

- 3D Boundary Element simulations, showing a power-law-dependency

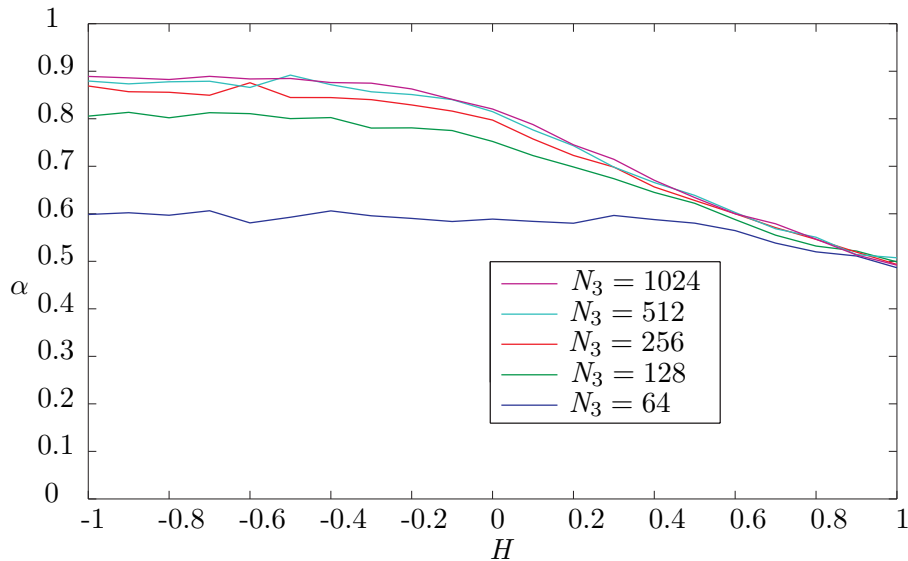


Figure 26: dependency of the exponent α for low H on the system size. Results have been obtained using 3D BEM with fast convolution technique, 500 samples for every data point.

- 1D MDR simulations, again showing a power-law-dependency
- analytical derivation, predicting power $\alpha(H)$

In both the numerical investigations, a dependency of α on H is observed. Figure 27 shows them all in one plot. I consider this particular plot the most important contribution of the current work. For details of α with $H < 0.2$, see fig. 26.

It can be seen that the runs of the curves are almost a perfect match. When working with the normalized variables introduced in eq. 4.13 and eq. 4.8, one can also find the prefactor ζ in the power-law 4.53. At the moment, I do not have an analytical expression for this prefactor, but numerical values from both MDR and BEM are available. These are shown in fig. 28. A fairly good approximation for ζ is given by $\zeta = \frac{1.7}{H+1}$. So eq. 4.53 can be expressed as

$$\bar{k} = \frac{1.7}{H+1} \bar{F}^{\alpha(H)}. \quad (4.74)$$

Knowing the prefactors allows us to adapt the 1D power spectrum even better. Instead of eq. A.73 we can assume a more general

$$C_{1D} = \lambda(H) q C_{2D}, \quad (4.75)$$

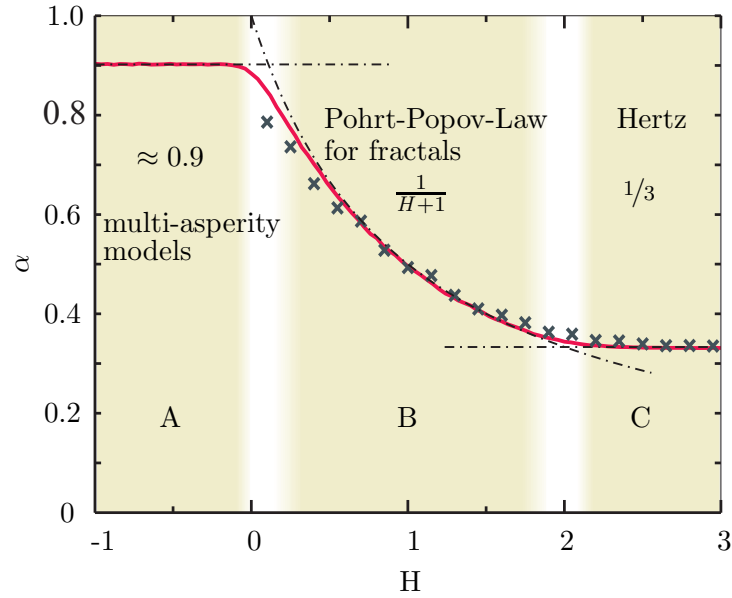


Figure 27: Numerical values for the exponent α from the power-law eq. 4.53, obtained using the 3D BEM (black crosses) as well as the 1D method of dimensionality reduction (red line).

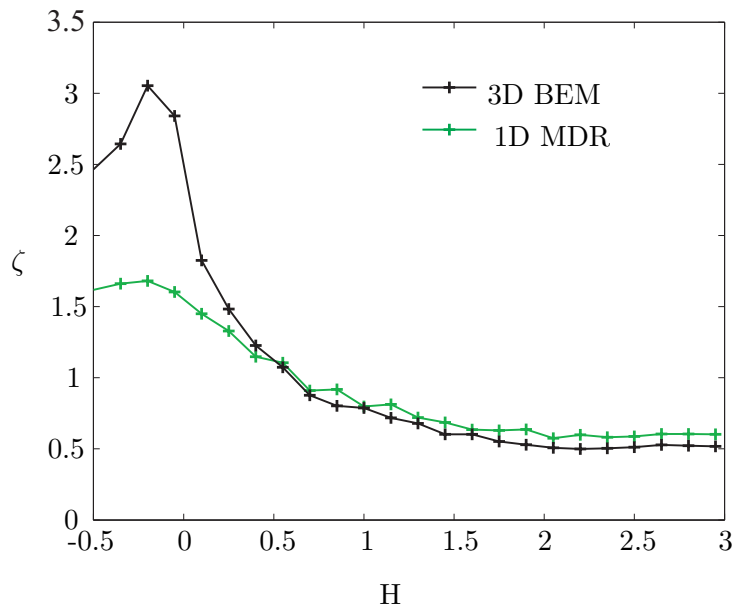
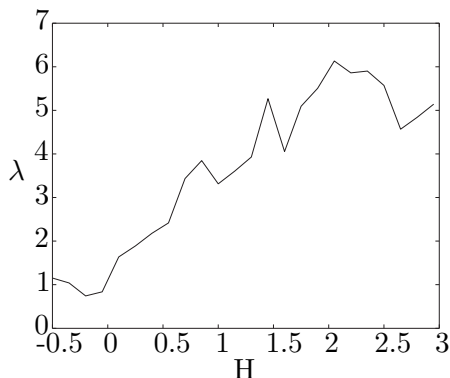


Figure 28: Numerical values for the prefactor ζ from the power-law eq. 4.53, obtained using the 3D BEM as well as the 1D method of dimensionality reduction.

Figure 29: prefactor λ from eq. 4.75.

which is inspired by eq. A.72. Fig. 29 shows this dependency in the best way I can currently extract it from numerical data. Using this prefactor to generate a rough line will result in the same asymptotical behavior as for the 3D equivalent, without the need to normalize to the rms roughness.

Even with the asymptotical runs of the curves being identical, a small discrepancy between 1D MDR and 3D BEM results can be observed. In the transition region from low to high forces, both simulations differ. Priority should be given to the 3D BEM results. Fig. 30 shows this transition region with numerical results from both BEM and MRD for different values of H , when curves coincide in the limit of low loads.

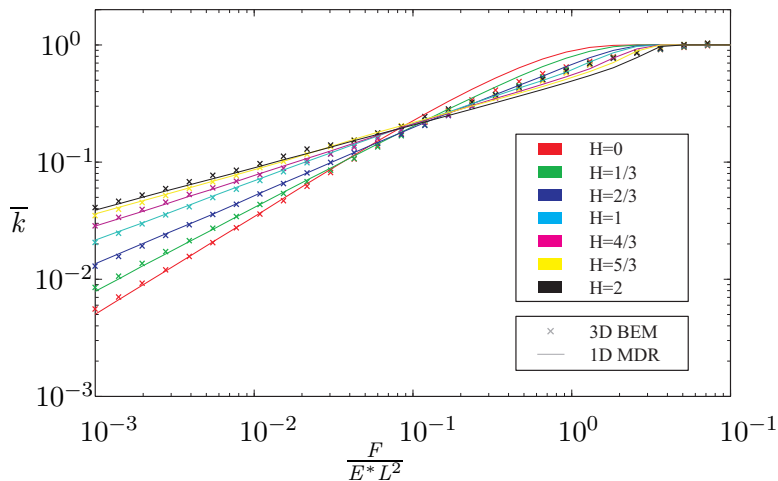


Figure 30: numerical results from 3D BEM and 1D MRD in the crossover region from power-law to constant stiffness. Some deviations can be found, which depend on the Hurst exponent.

4.6 Comparison to previous models

The power-law dependency 4.31 $\bar{k} \propto \bar{F}^{\alpha(H)}$ has been found earlier in related works with different exponents. In [16], Ciavarella et. al. included interaction in the Greenwood-Williamson model and compared the results to the original model. They found that the force-stiffness-relation “generally is less than linear”. The nonlinearity was discovered to be more pronounced for $H \approx 1$ than for $H \approx 0$. This is in accordance with the findings of $\alpha = (H + 1)^{-1}$. Figures 32 and 31 show the data presented in [16] for $H = 0.95$ and $H = 0.05$ together with the slope predicted by eq. 4.31. It can be seen that for H in the vicinity of 1, very good agreement to the improved GW-model (including interaction) can be found. For $H \approx 0$, the power $1/(H + 1) \approx 0.9524$ does not fit as well, but is clear that by using $1/(H + 1)$, I overestimate the power by not taking into account the resolution dependence, see fig. 25. Paggi and Barber [50] find a weak dependency of the exponent on the fractal dimension in a numerical study. Fig. 33 shows their data for low forces (see Fig. 7b of the original paper) together with the corresponding slopes from eq. 4.31.

As a reaction to the results of this chapter being published [61] [63], Pastewka et. al. [51] imitated the numerical experiments and formulated a similar derivation for $\alpha = 1/(H + 1)$. They confirmed both the numerical results and the analytical expression.

The surfaces treated here are not nominally flat. Even at the largest scale, they have a pronounced roughness, making them effectively a single large indenter. A direct comparison to studies treating flat surfaces is thus not suitable. The next section will suggest a way to consider these surfaces using the current model.

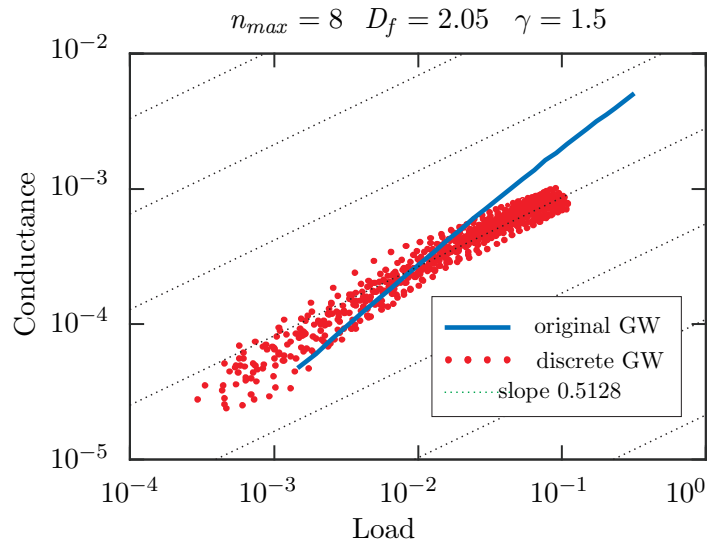


Figure 31: Contact conductance (stiffness) as a function of load in the frame of the classical Greenwood-Williamson model (blue line) and for an improved model including asperity interaction at 25 surface realizations (red spots). Courtesy of M.Ciavarella [16]. Green dashed slope according to $\alpha = (4 - D_f)^{-1}$ eq. 4.31. All data is for $D_f = 2.05$, so $H = 0.95$. Very good agreement between the improved discrete GW model and the corresponding slope from eq. 4.31 can be found, while the original GW model has a qualitatively different behavior (linear).

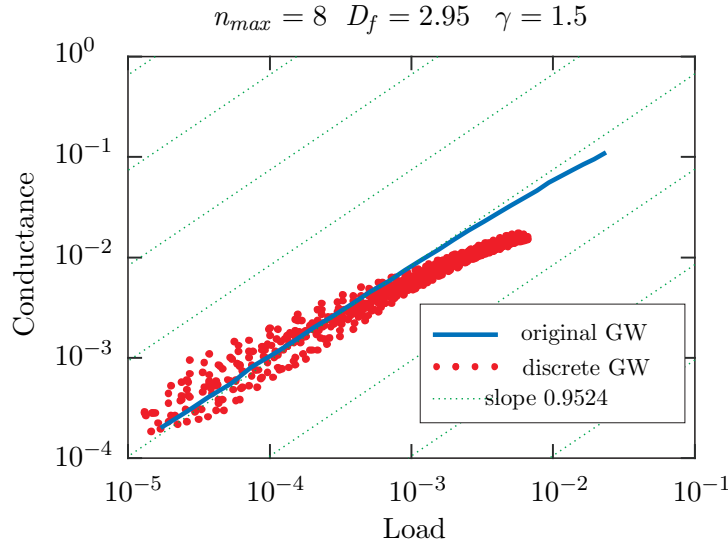


Figure 32: Contact conductance (stiffness) as a function of Load in the frame of the classical Greenwood-Williamson model (blue line) and for an improved model including asperity interaction at 25 surface realizations (red spots). Courtesy of M.Ciavarella [16]. Green dashed slope according to $\alpha = (4 - D_f)^{-1}$ eq. 4.31. All data is for $D_f = 2.95$, so $H = 0.05$. The slope is slightly overestimated, due to the resolution dependence for low H , see fig. 25.

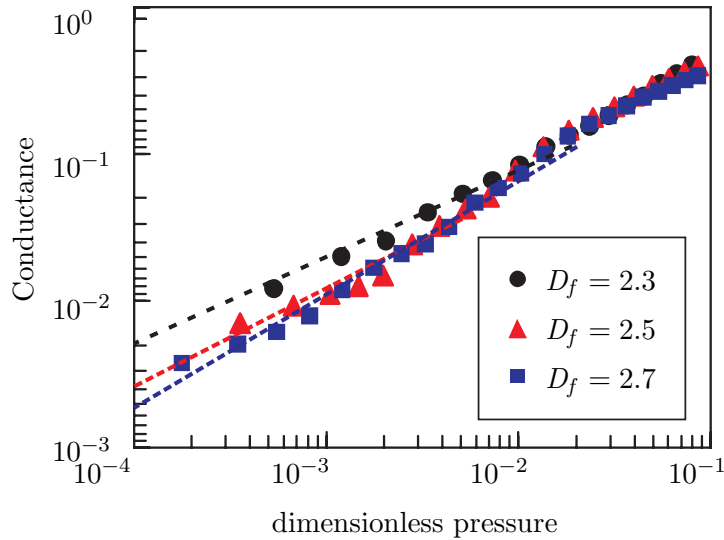


Figure 33: Effect of D_f on the dimensionless specific contact conductance as a function of the dimensionless pressure. Courtesy of M.Paggi [50]. Colored dashed slopes according to $\alpha = (4 - D_f)^{-1}$ eq. 4.31. For small forces, a power-law is observed with an exponent close to the analytical prediction.

5 Applications

5.1 Application to nominally flat fractal surfaces

The findings of the previous chapters may also be applied to estimating the contact stiffness of randomly rough, but nominally flat surfaces. Especially for $H > 0.5$, the results given basically describe a single indenter, while many practical applications include the contact of nominally flat surfaces. Take for example a sandblasted surface with no macroscopic curvature. The roughness on this surface may not have any roughness with wavelength considerably longer than the grain size. From the power spectrum, these surfaces are characterized by either a Cut-Off or a Roll-Off, see fig. 34.

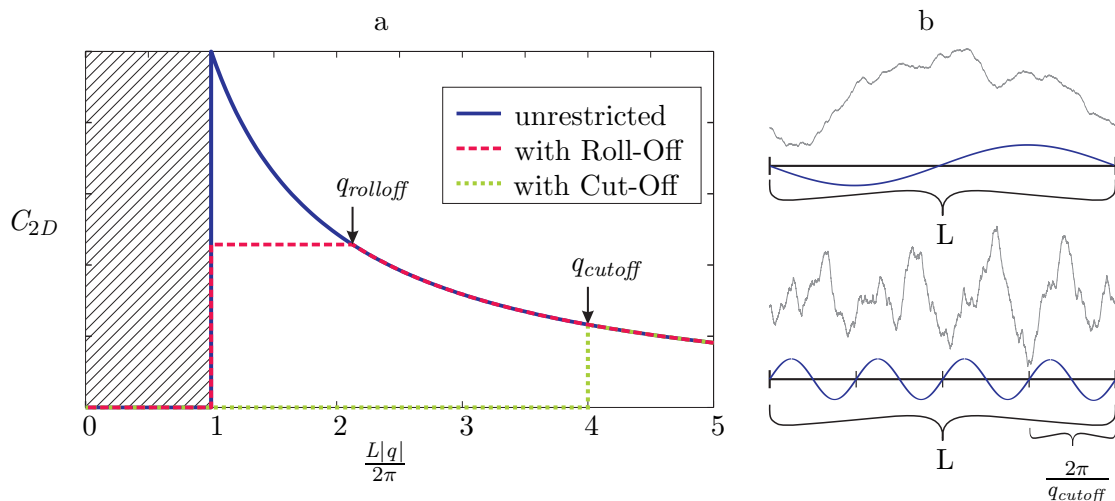


Figure 34: Explanation of the Roll-Off and Cut-Off in fractal surfaces. (a) general power spectrum of surface with and without cut-Off/Roll-Off. All follow the the power-law eq. 2.8, but have different behavior in the long-wavelength region. (b) Examples of rough lines, the upper one being unrestricted fractal. The lower one has a Cut-Off at the indicated wavelength and is thus nominally flat.

The case of surfaces with *Roll-Off* has already been addressed in the previous chapters, because it corresponds to a Hurst exponent of $H = -1$. Here we expect $k \propto F^\alpha$ with $\alpha \approx 0.9$.

That leaves us with surfaces of the *Cut-Off*-type. As can be seen from fig. 34b, the surface which has a cut-off effectively consists of multiple local maxima, which are separated from each other by a characteristic distance of $\lambda_{cutoff} = 2\pi/q_{cutoff}$. Also, it can be seen that the highest points of these local maxima differ in height.

Let us now introduce two assumptions:

- Elastic coupling for distances greater than λ_{cutoff} is negligible
- the height distribution of local maxima follows an exponential distribution

In this case we end up with a multi-asperity model as described in 3.1. The behavior of an individual spring in this model is now the behavior of on single λ_{cutoff} -asperity, as described by the Pohrt/Popov power law, which can also be expressed as

$$F(d) \propto d^{\frac{H+1}{H}}. \quad (5.1)$$

This is exactly what we required in eq. 3.2. Of course $\frac{H+1}{H} > -1$ for all $0 \leq H < 2$, in particular for the physically most relevant region of $H \approx 1$. As in chapter 3.1, we can find the contact stiffness to be proportional to the normal force for fractal rough surfaces that have a considerable Cut-Off.

This finding is especially interesting as it demonstrates the compatibility of the current work with the works of Persson, Müser, Pastewka and coworkers who insisted on this point for nominally flat surfaces. Initially, it was thought that there was a great discrepancy.

5.2 Application to curved bodies

In the previous section, we have seen how the very basic case of an unrestricted fractal roughness feature can be used in order to solve or predict the behavior of nominally flat surfaces in contact. A similar problem of great practical importance is that of a rough non-conforming curved contact. The idea is to extend the Hertzian solution of perfectly smooth spheres to rough but nominally curved bodies. Numerous practical applications exist for this problem, the most prominent being ball-bearings, possibly with signs of wear. For these systems, I will show that there is a pronounced crossover from the behavior which is typical for the fractal surfaces to Hertz-like behavior and derive an analytical approximation for the entire range of forces. The findings of this chapter have also been published in [62].

Consider a rigid rough spherical indenter with the radius R , which is approximated by a superposition of a parabolic shape $z_p(x, y) = \frac{x^2+y^2}{2R}$ and a random self-affine roughness $z_r(x, y)$ with the Hurst Exponent H . A sample of such a rough sphere is shown in fig. 35.

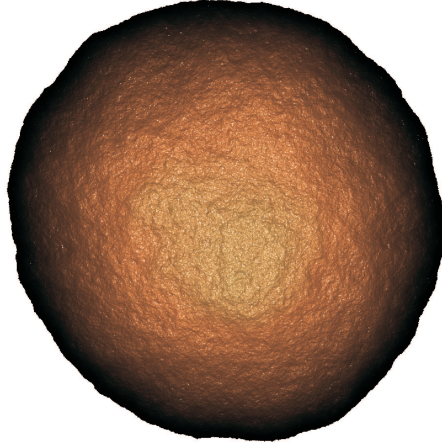


Figure 35: Numerically generated rough sphere, $H = 0.7$.

Analogy of fractal roughness and rotational indenter shapes

For now let us focus on the indentation behavior of the roughness z_r only. Assuming that the roughness features the self-affinity property eq. 2.1, the magnification of the surface "looks" just as the original. Interestingly, this is also the case for a radially symmetric indenter with its shape given by

$$z_s(r) = Q_{3D} \cdot |r|^H. \quad (5.2)$$

Not only does the indenter shape eq. 5.2 feature the fractal property, another interesting fact links it to the fractal roughness. In [20],[78],[23] it was shown that for the indentation of this indenter shape into the elastic half-space, the following expression is valid for the normal contact stiffness k and the normal force F :

$$\frac{\partial F}{\partial d} = k = 2E^* \left(\frac{(H+1)F}{2Q_{3D}E^*H\kappa(H)} \right)^{\frac{1}{H+1}} \propto F^{\frac{1}{H+1}}. \quad (5.3)$$

For all these indenter shapes z_s , the contact stiffness k is proportional to the normal force F in power $(H+1)^{-1}$. For example, the Hertzian contact is one particular case of this formulation with $H = 2$ and $Q_{3D} = 1/2R$ giving the classical result

$$\frac{k}{E^*} = \left(6R \frac{F}{E^*} \right)^{\frac{1}{3}}. \quad (5.4)$$

For fractal rough surfaces the dependency reads

$$\frac{k}{E^*L} = \frac{1.7}{H+1} \left(\frac{F}{E^*hL} \right)^{\frac{1}{H+1}} \propto F^{\frac{1}{H+1}}. \quad (5.5)$$

So a rotationally symmetric indenter with power H has the same indentation behavior as a fractal rough surface which is characterized by its Hurst Exponent H . By comparing k in eq. 5.5 and eq. 5.3, the prefactor Q_{3D} necessary to establish the equivalence between both must read

$$Q_{3D} = \left(\frac{2}{\zeta L} \right)^{H+1} \frac{(H+1)Lh}{2H\kappa(H)}. \quad (5.6)$$

The equivalence of a rotational symmetric indenter and a rough surface only holds for the average value of multiple random rough realizations. The fact that surfaces have random phases can make them differ in their stiffness behavior. A deviation of about 30% is observed (see fig. 18). The radially symmetric system of course is deterministic and has no fluctuations.

Analytical solution to the analogous problem

With this insight, instead of superpositioning the parabolic shape z_p with the rough surface z_r , we superposition z_p with the equivalent rotational symmetric shape z_s ,

$$z_c = z_p + z_s, \quad (5.7)$$

$$z_c(r) = \frac{r^2}{2R} + \left(\frac{2}{\zeta L} \right)^{H+1} \frac{(H+1)Lh}{2H\kappa(H)} |r|^H. \quad (5.8)$$

Figure 36 (c) shows a cut through the resulting 3 dimensional, rotational symmetric indenter shape.

For the indentation of this combined shape, the dependence between normal force and normal contact stiffness can again be found using the solution by [20],[78]:

$$F(k) = E^* \left[\frac{1}{6R} \left(\frac{k}{E} \right)^3 + Lh \left(\frac{k}{\zeta EL} \right)^{H+1} \right]. \quad (5.9)$$

This relation can also be found very elegantly using the method of dimensionality reduction, see [29]. For small values of the normal force or the contact stiffness we expect to see the behavior according to eq. 5.5, while at higher forces (higher stiffness, deeper indentation) the Hertzian behavior eq. 5.4 is predicted. The crossover is expected to

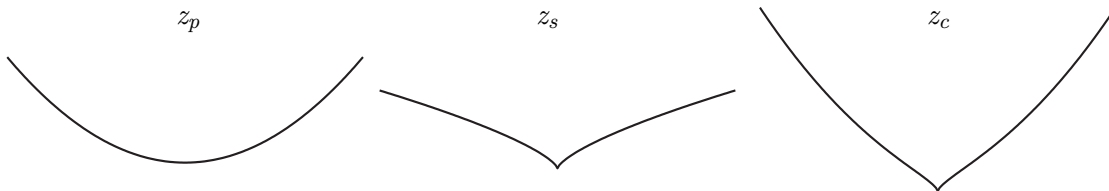


Figure 36: (a) parabolic shape z_p (b) indenter shape z_s according to eq. 5.8 with $H = 0.7$ (c) superposition z_c of both.

take place at the intersection of both

$$\frac{F}{E^*} = \left[\zeta(H)^{3H+3} h^{-3} L^{3H} (6R)^{-H-1} \right]^{\frac{1}{H-2}}. \quad (5.10)$$

This dependence is show in fig. 37 together with the numerical results from the next section.

Numerical Solution for the original problem

Independently from the analytical considerations above, numerical studies were conducted using the 3D boundary element method. A total of 50 samples similar to fig. 35 were generated using the inverse Fourier transform and superposed to a parabolic shape. The large number of samples is needed for giving adequate statistics because fluctuations occur due to the random nature of the roughness. All samples were generated on a grid of 513×513 discrete, evenly spaced points. For a series of normal force values, the contact stiffness was solved.

Fig. 37 shows the resulting dependency with red dots. For small normal forces, the system is dominated by the roughness and the stiffness approaches eq. 5.5. For higher normal forces, the influence of the roughness vanishes and the system behaves like a smooth spherical Hertzian indenter. When such a rough indenter is treated as purely Hertzian, then the contact stiffness can only be *overestimated*.

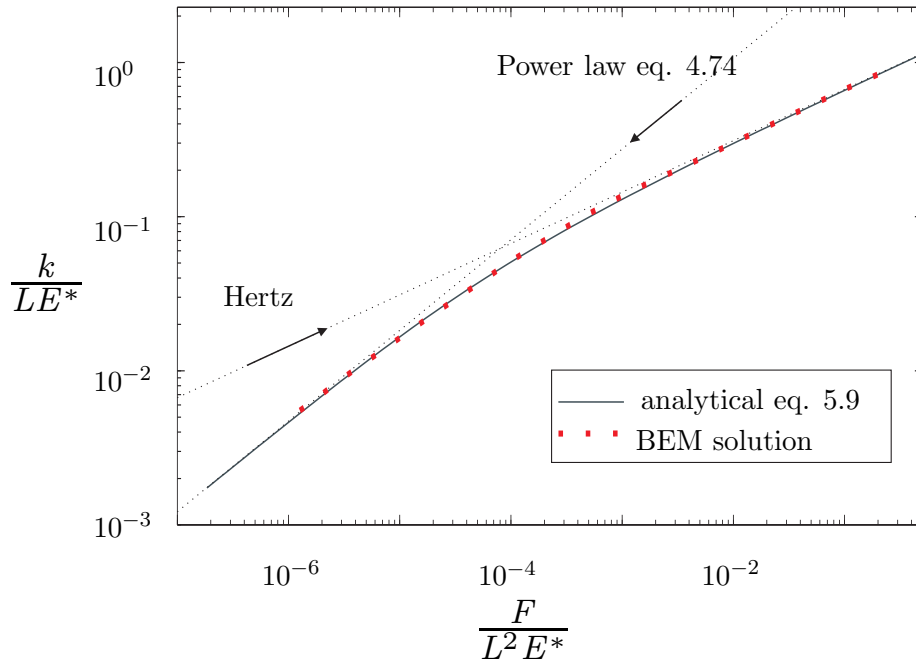


Figure 37: Normalized normal Force und normal stiffness for a spherical indenter, superposed with a random roughness ($R = 0.5$, $H = 0.7$, $L = 1$, $h = 9 \cdot 10^{-3}$). The red line is the results of a 3D boundary element study. The wide dotted line ist the theoretical prediction according to eq. 5.9. Furthermore, the asymptotical behavior of the plain roughness eq. 5.5 and the smooth Hertzian case eq. 5.4 is shown. The slope of the asymptotes is $1/3$ in the Hertzian case and $(H + 1)^{-1}$ for the roughness. The crossover occurs at $\frac{F}{L^2 E^*} = 8 \cdot 10^{-5}$, see eq. 5.10.

6 Conclusion

The present work treated the indentation of a fractal rough surface into the elastic half space. Special emphasis was put on the normal contact stiffness, because it has analytical proportionalities to other relevant quantities in contact.

For the case of “pure” fractal surfaces i.e. surface with no restriction of the fractal law in their power-spectrum, it was found that the contact stiffness \bar{k} rises with the normal force \bar{F} in a power-law fashion

$$\bar{k} \propto \bar{F}^\alpha. \quad (6.1)$$

The exponent α generally depends on the fractal parameter H , but in the case of H smaller than approx. 0, depends on the number of scales for which the fractal power-spectrum holds. This small-scale-limit may be greater than or equal to the numerical resolution. In the most relevant region of approximately $0 < H < 2$, a new analytical expression is found. This is the central finding of the present work:

$$\alpha = \frac{1}{H + 1}. \quad (6.2)$$

Seamlessly, this dependency transitions into $\alpha = 2/3$ for $H \geq 2$, which corresponds to the classical Hertzian case of single sine asperity.

A closed expression of the prefactor for eq. 6.1 has not been found yet, but numerical approximation data is presented in fig. 28.

Non-restricted (“pure”) surfaces of the fractal type with H in the vicinity of 1 do not correspond to nominally flat surfaces, instead these are more like a single rough indenter. Therefore, the linear relation between normal force and normal stiffness found by different previous models (see sec. 3) does not apply. In order to analyze flat surfaces restricted by a cut-off or roll-off, sec. 5.1 suggests that they should be seen as multiple independent asperities of the unrestricted type, see sec. 4.4.1. For that case follows that the contact stiffness rises with the normal force in a linear way.

The results of α and its dependencies on H and the number of modes have been found analytically and using two radically different numerical methods. The applicability of the method of dimensionality reduction (MDR) for rough surfaces has been demonstrated for the first time. The results of the present work have been published in several papers [61][63][60][59][62][58] and as a chapter of the book [67].

7 Outlook

The results of this work have direct implications to other problems in tribology, some of which I want to address here.

The power-law 4.74 can be reformulated knowing that the fractal rough surfaces satisfy

$$h = \Theta L^H. \quad (7.1)$$

So we can write with one parameter Θ instead of both L and h :

$$\frac{k}{E^*} = \zeta \left(\frac{F}{E^* \Theta} \right)^{\frac{1}{H+1}}. \quad (7.2)$$

As we know from sec. 4, eq. 4.2, the electrical conductivity Λ_e and the heat conductivity Λ_t 4.4 have exact proportionalities, which can now be expressed as a function of F with the help of eq. 7.1:

$$\frac{k}{E^*} = \frac{1.7}{H+1} \left(\frac{F}{E^* \Theta} \right)^{\frac{1}{H+1}} = \Lambda_e \frac{(\rho_1 + \rho_2)}{2} = \Lambda_t \frac{2}{(\lambda_1 + \lambda_2)}. \quad (7.3)$$

The findings for the normal contact stiffness can also be applied to the lateral stiffness. As we have seen in sec. 4, if two bodies with equal elastic properties are in a non-sliding circular contact with an arbitrary radius, then the ratio of the normal contact stiffness k_z to the tangential contact stiffness k_t is given by the Cattaneo-Mindlin factor C_m eq. 4.5

$$\frac{k_z}{k_t} = \frac{2 - \nu}{2(1 - \nu)} =: C_m, \quad (7.4)$$

where ν is the Poisson's ratio of the material. This relation was originally found for circular contact spots [45] and was later confirmed numerically [14] for isotropic, self-affine, nominally flat surfaces. Using 7.2 we directly find

$$\frac{k_t}{E^*} = \frac{2(1 - \nu)}{2 - \nu} \zeta \left(\frac{F}{E^* \Theta} \right)^{\frac{1}{H+1}}. \quad (7.5)$$

This analogy can be extended from non-slipping contacts to tangentially loaded contacts that are just about to start slipping [76][7]. In [27], it is shown how eq. 7.2 can be used to estimate the maximum lateral displacement $u_{x,max}$ of a rough indenter before the

state of macroscopic slipping starts:

$$u_{x,\max} = \mu C_m Z \left(\frac{F}{E^*} \right)^{\frac{H}{H+1}}. \quad (7.6)$$

Z is a constant

$$Z = \frac{H + 1}{0.2055H} (0.086\Theta)^{\frac{1}{H+1}} \quad (7.7)$$

and μ is the macroscopic coefficient of friction. This simple estimation thus shows that the maximum displacement before macroscopic slip depends on the normal force in a power-law fashion, but does not depend on the system size.

The simplicity of the newly found relation between normal force and stiffness and thus more adjacent quantities in tribology opens up a new viewpoint and the possibility to investigate other problems in contact mechanics using the given approach.

Closely related to the work done so far, some questions still remain open to further research

- Can we find the prefactor ζ analytically? For small values of H it will surely depend on the system size in addition to the other parameters. In this context it seems favorable to use the normalization according to eq. 7.2.
- Can some of the ideas be used in estimating the contact area, not only as function of the applied load, but also on grid resolution / short wave cut-off?
- How do other types of rough surfaces behave under increasing load? It would be of special interest to see finite bodies with free boundaries and nominally flat surfaces with varying low wavelength cut off. A high amount of computational capacity will be necessary for such investigation but it can be handled.
- Dozens of similar interesting problems can be tackled with an implementation of the high-efficiency BEM A.1.2 being applied not only to the Boussinesque normal solution, but also to the Cerrutti-solution of tangential loading. Both together could be used to study the transition from sticking to slipping for randomly rough and other surface shapes.
- Is there a way to improve the convergence rate of the underlying CG-based method in the BEM? Can a modified relaxation step help?

7 OUTLOOK

Some of the above mentioned topics have been addressed already, others are subject to current research. With analytical tribology being a relatively young area of research, there is still a lot to discover.

A Appendix

In this appendix I want to give some details on the numerical methods that were used in the current work. Most of methodologies presented here have been published before by other authors, in which case I will give a review of the basic idea and try to give reference to both the analytical background and implementational details. Special emphasis is brought to the boundary element method for the following reasons:

- The method is very popular among contact mechanists
- The method of Multi-level-Multi-integration (MLMI) is very fascinating and yet little known
- The MLMI or Fast Convolution together with the CG-method can also be applied to tangential problems, again only solving surface deflections.
- There is a way to easily formulate the BEM for rotational symmetric contact problems.

To my best knowledge, the last point has never been published before. It may seem of little use – the normal contact problem for rotationally symmetric indenter shapes has been solved already by Galin and Sneddon [20],[78],[23] and also in the frame of the reduction method by Heß [28], but both are only applicable to circular contact regions, while the BEM also allows for ring-shaped contact areas.

A.1 BEM

The Boundary Element method is a great tool in numerical contact mechanics. It allows to calculate the surface deflections without discretizing the inner space of the contacting bodies and can be applied whenever the half-space-approximation is valid, see sec. 1.

In the case of non-conforming curved surfaces, the problem consists not only of finding the correct contact pressures and corresponding deflections, but also include finding the true area of contact in the first place. As this partitioning is not known a priori, it must be detected in an iterative procedure in the frame of the boundary element method. This procedure should also be applied when the surface topography is known, for example from measurements. In this case, the BEM is a deterministic tool for solving the contact behavior of the particular surface, which is important because only so many contact theories exist (see sec. 3 and the contribution from this current work). The partitioning of the apparent area of contact can also be applied to lubricated contacts, saying whether

a local spot is in direct material contact or separated by a fluid film. In this case, the non-contacting regions will still possess a positive contact pressure due to the lubricant. When treating the problem of two long parallel cylinders in contact, the deflections are not the same as in the classical 3D case. Instead, the case of an infinite line contact applies. The case of smooth cylinders has been solved by Hertz [31], but incorporating the "line contact" case into the BEM will allow us to investigate other two-dimensional indenter shapes. Furthermore, the 2D line contact deflections as a function of the Force per length (which substitutes pressure in this case) is needed for the calculation of the elastohydrodynamic lubrication, for examples in wide gear teeth. Here, the gap width resulting from the surface deflection is adjusted iteratively until it fits with a the pressure distribution resulting from the Reynolds equation in that gap.

The last case is the one of a rotational symmetric contact problem. It is somewhat academic in most cases and solutions exist for the dry contact [78] [28], but similar to the elastohydrodynamic lubrication problem, the role of intermediate layer between surfaces and their squeeze-out behavior can be investigated using this approach, while taking into account the elastic deformations of the bulk bodies. This problem appears in nanoimprinting processes [48] and is related to the rolling contact of rail and wheel [70].

For the general understanding, it is helpful to imagine one of the surfaces (WLOG the upper) to be shaped and stiff, while the other surface is smooth and elastic. When initially both bodies were curved or rough, then the shape of the upper bodies is chosen to give the same gap width. Considering only the correct gap width instead of both surface shapes is legitimate as long as the half-space approximation is valid, which also demands for the contacting bodies to be large in comparison to the dimensions of the contact area.

General methodology for dry contact

At the beginning of a numerical study, the shape of the resulting contact area is not known, but we know the following assumptions to be true for the zones of contact and those of no-contact.

- Wherever the bodies are in contact, the gap width is zero and the contact pressure is positive.
- In the zones of no-contact, the gap width is positive and the contact pressure vanishes

Which leads to following unknowns:

- the pressure inside the contact area
- the gap width on the outside

This problem can be treated numerically. As we assume linear elasticity, is it sensible to formulate the following linear equation for the relation of the discrete values of pressure p and displacement u , given by the matrix A

$$u = Ap. \quad (\text{A.1})$$

In chapter A.1.1, we will see how to find the matrix A for the different geometrical cases. Consider the following procedure described in [21]. We assume some initial partitioning into areas in-contact (i) and those out-of-contact (o). So for the deflection u and pressures p we know

$$p_i > 0, \quad (\text{A.2})$$

$$p_o = 0, \quad (\text{A.3})$$

$$u_i = z_{1,i} - z_{2,i}, \quad (\text{A.4})$$

$$u_o > z_{1,i} - z_{2,i}. \quad (\text{A.5})$$

So that conditions A.4 and A.3 are known. We can now sort the discrete points in A.1 to give:

$$\begin{bmatrix} A_1 & A_2 \\ A_3 & A_4 \end{bmatrix} \begin{Bmatrix} p_i \\ 0 \end{Bmatrix} = \begin{Bmatrix} u_i \\ u_a \end{Bmatrix}. \quad (\text{A.6})$$

We can express this equation as:

$$A_1 p_i = u_i, \quad (\text{A.7})$$

$$A_3 p_i = u_a. \quad (\text{A.8})$$

Equation A.7 is suitable for solving p_i , the pressure inside the contact area. Using A.8 and this pressure, one can then determine the deflections outside the contact area. If the preassumed contact area and partitioning was correct, then the contact problem is solved. Whether or not the partitioning was correct can be seen from testing conditions A.2 and A.5. Any discrete point that fails these condition must change status (be included or

excluded from the contact area). With the new contact area, the whole process starts anew, until no negative contact pressures or negative gap widths are found.

This approach can thus be solved, using only standard method of linear algebra. With equidistant grid spacing, we can make A from eq. A.1 independent from the grid spacing Δ and the elastic constants such as $E^* = \frac{E}{(1-\nu^2)}$ (the latter only in the case of normal contact)

$$A = \frac{\Delta}{\pi E^*} B. \quad (\text{A.9})$$

The advantage of this formulation is the fact that matrix B may be precalculated and stored, because it is independent of the problem size/grid spacing.

In the following section we will seek to find matrix B for the different geometrical configurations.

A.1.1 Formulation for different geometric scenarios

3D

Boussinesq first investigated the problem, what stresses and deformations occur inside the elastic half-space, when loaded by a concentrated normal force at a single spot. With the force acting at the point of origin, the solution in cylindrical coordinates reads

$$u_r = \frac{P}{4\pi GR} \left[\frac{rz}{R^2} - \frac{(1-2\nu)r}{R+z} \right], \quad (\text{A.10})$$

$$u_\theta = 0, \quad (\text{A.11})$$

$$u_z = \frac{P}{4\pi GR} \left[2(1-\nu) + \frac{z^2}{R^2} \right]. \quad (\text{A.12})$$

Here $R^2 = r^2 + z^2$ and G is the modulus of shear. If the surface is loaded with a pressure distribution $p(x, y)$ then the surface deflection can be integrated as

$$u_z(x, y, z = 0) = \frac{1}{\pi E^*} \iint_{(F)} \frac{p(\hat{x}, \hat{y})}{\sqrt{(\hat{x}-x)^2 + (\hat{y}-y)^2}} d\hat{x} d\hat{y}. \quad (\text{A.13})$$

In the discrete case with both x and y having equidistant grid spacing Δ and the total system size being $N \times N$ points, the following discrete formulation for the deflection u_{ij} as a function of the pressures p_{ij} can be used:

$$u_{ij} = \frac{\Delta}{\pi E^*} \sum_{\hat{i}=1}^N \sum_{\hat{j}=1}^N K_{ij\hat{i}\hat{j}} p_{\hat{i}\hat{j}}. \quad (\text{A.14})$$

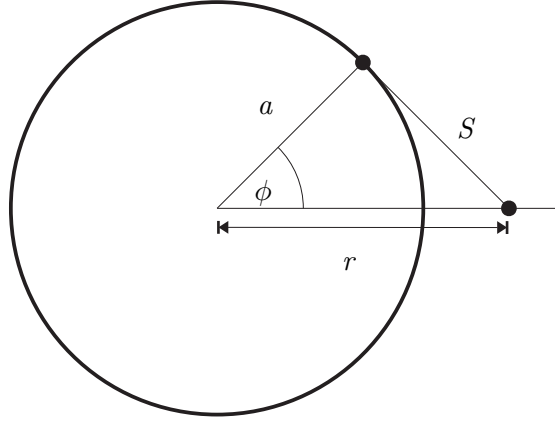


Figure 38: Radial symmetric distribution of a Force on a thin circular ring

where

$$K_{ij\hat{i}\hat{j}} = \left[a \ln \frac{c+\sqrt{a^2+c^2}}{d+\sqrt{a^2+d^2}} + b \ln \frac{d+\sqrt{b^2+d^2}}{c+\sqrt{b^2+c^2}} + c \ln \frac{a+\sqrt{a^2+c^2}}{b+\sqrt{c^2+b^2}} + d \ln \frac{b+\sqrt{b^2+d^2}}{a+\sqrt{a^2+d^2}} \right] \quad (\text{A.15})$$

and

$$a = i - \hat{i} + \frac{1}{2}, \quad b = i - \hat{i} - \frac{1}{2}, \quad c = j - \hat{j} + \frac{1}{2}, \quad d = j - \hat{j} - \frac{1}{2}. \quad (\text{A.16})$$

In order to find matrix B from K , the values of p_{ij} and u_{ij} must be rearranged into a column-matrix in some suitable way and then the 4-parameter array $K_{ij\hat{i}\hat{j}}$ can be rearranged accordingly to give B .

It should be noticed that matrices K and B are very regular and very large in size (N^4), but only contains $\frac{N^2}{2}$ unique values. In sec. A.1.2 we will see methods that take advantage of these properties in order to save computational time and memory.

Radial symmetric

For the case of a radial symmetric indenter, lets us again consider a concentrated force, acting on a base element, in this case a thin circle. This is the starting point for a radial symmetric pressure distribution. The deflection at a point r reads (See Appendix of

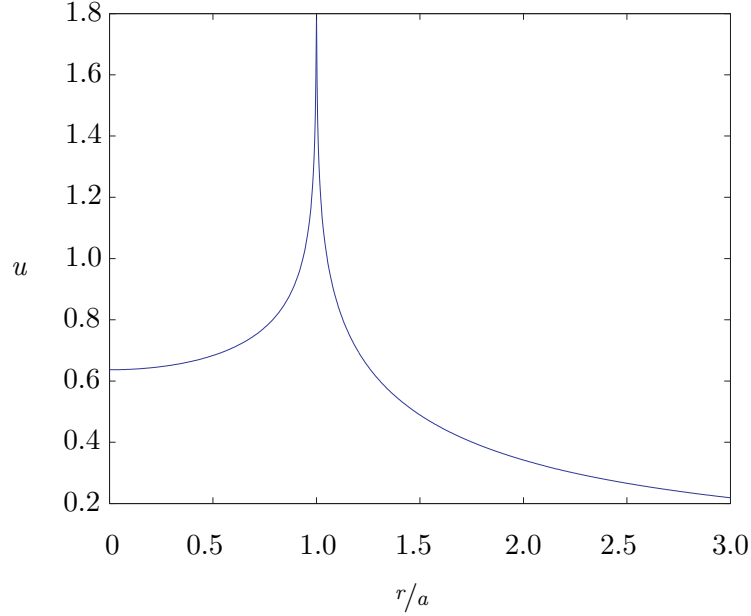


Figure 39: Surface deflecting for a ring-shaped force.

[70])

$$u_z = \frac{1}{\pi E^*} \int_0^{2\pi} \frac{F_N}{2\pi S} d\phi \quad (\text{A.17})$$

$$u_z = \frac{1}{\pi E^*} \int_0^{2\pi} \frac{F_N}{2\pi} \frac{1}{\sqrt{a^2 + r^2 - 2ar \cos \phi}} d\phi \quad (\text{A.18})$$

$$u_z = \frac{F_N}{aE^*} \frac{2}{\pi^2 \left(1 + \frac{r}{a}\right)} K \left(2 \frac{\sqrt{\frac{r}{a}}}{1 + \frac{r}{a}} \right). \quad (\text{A.19})$$

Here $K(\kappa)$ is the complete elliptic integral of the first kind

$$K(\kappa) = \int_0^{\frac{\pi}{2}} \frac{1}{\sqrt{1 - \kappa^2 \sin^2 \phi}} d\phi. \quad (\text{A.20})$$

Fig. 39 shows the resulting displacement with prefactor $\frac{2aE^*}{F_N}$. In the vicinity of $r = a$ there is a logarithmic singularity, which can be approximated as [70]

$$u_z = \frac{F_N}{\pi^2 a E^*} \ln \frac{8}{\left| \frac{r}{a} - 1 \right|}. \quad (\text{A.21})$$

For our further inquiries we will need the continuous dependence on the contact pressure. Let us thus assume a homogenous pressure distribution P on a circular ring whose width

is given by Δ . Then we obtain for the deflection u_z

$$F_N = A_{ring} P \quad (\text{A.22})$$

$$F_N = P (2a + \Delta) \Delta \pi \quad (\text{A.23})$$

$$F_N \approx P 2a \pi \Delta. \quad (\text{A.24})$$

So we can define a deflection function u_0 :

$$u(r, a) = \frac{\Delta P}{\pi E^*} u_0(r, a), \quad (\text{A.25})$$

$$u_0(r, a) = \begin{cases} 2 \ln \frac{8}{\left| \frac{r}{a} - 1 \right|} & \left| \frac{r}{a} - 1 \right| \ll 1 \\ \frac{4}{\left(1 + \frac{r}{a}\right)} K \left(2 \sqrt{\frac{r}{1 + \frac{r}{a}}} \right) & \text{otherwise} \end{cases}. \quad (\text{A.26})$$

With a given pressure distribution $P(r)$ the local displacement at radius r reads

$$u(r) = \frac{\Delta}{\pi E^*} \int_0^\infty P(a) u_0(r, a) da. \quad (\text{A.27})$$

When the pressure is given as discrete values, one can interpolate $P(a)$ in between. There is even a elegant way to include this in the actual integration. Consider an equidistant grid \bar{R} with $R_0 = 0$ and $R_N = r_{max}$ with grid spacing Δ , such that $R_j = j \Delta$. Consider an elementary pressure distribution E_k as in fig. 40

$$E_k(x) = \begin{cases} 1 - \frac{|x - R_k|}{\Delta} & \text{for } R_{k-1} \leq x \leq R_{k+1} \text{ and } 0 \leq x \leq r_{max} \\ 0 & \text{otherwise} \end{cases}. \quad (\text{A.28})$$

This vector of functions has the neat property to interpolate the pressure values when multiplied (dot product) with the pressure values.

$$\bar{P} \bullet \bar{E}(x) = P_{lin}(x) \quad (\text{A.29})$$

where $P_{lin}(x)$ is the linear interpolation of the discrete Pressure \bar{P} . So we replace $P(a)$

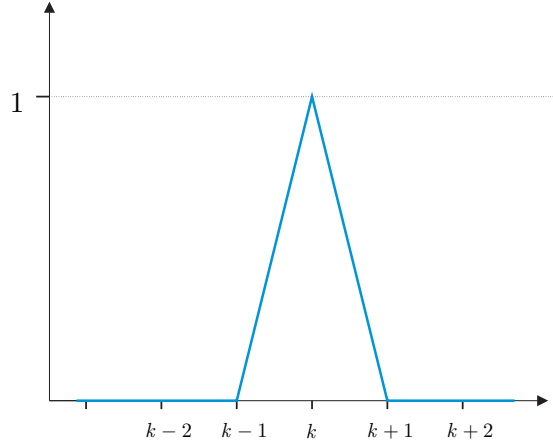


Figure 40: elementary pressure distribution to help with the linear interpolation.

by $\overline{P} \bullet \overline{E}(a)$

$$u(r) = \frac{\Delta}{\pi E^*} \int_0^{\infty} \overline{P} \bullet \overline{E}(a) u_0(r, a) da, \quad (\text{A.30})$$

$$u(R_j) = \sum_{i=1}^N \left[\frac{\Delta}{\pi E^*} \int_{R_{i-1}}^{R_{i+1}} \overline{E}_i(a) u_0(R_j, a) da \right] P_i. \quad (\text{A.31})$$

Please note that $u_0(r, a)$ is a function of the quotient $\frac{r}{a}$ only. Inserting $R_i = i\Delta$ we can write

$$u_j = \sum_{i=1}^N \left[\frac{\Delta}{\pi E^*} \int_{\Delta(i-1)}^{\Delta(i+1)} \overline{E}_i(a) u_0(j\Delta, a) da \right] P_i, \quad (\text{A.32})$$

$$u_j = \sum_{i=1}^N \left[\frac{\Delta}{\pi E^*} \int_{i-1}^{i+1} E_i(\Delta a) u_0(j, a) da \right] P_i. \quad (\text{A.33})$$

With the shorter boundaries, we can express $E_i(\Delta a)$ without considering two cases for

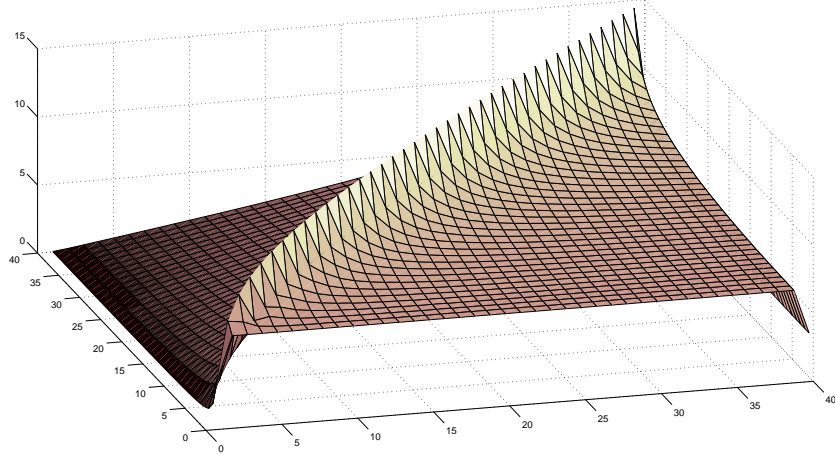


Figure 41: deflection matrix in the radial symmetric case, $N = 40$

$i \in [2 \dots N - 1]$:

$$u_j = \sum_{i=1}^N \left[\frac{\Delta}{\pi E^*} \int_{i-1}^{i+1} \left(1 - \frac{|(\Delta a) - R_i|}{\Delta} \right) u_0(j, a) da \right] P_i, \quad (\text{A.34})$$

$$u_j = \sum_{i=1}^N \left[\frac{\Delta}{\pi E^*} \int_{i-1}^{i+1} (1 - |a - i|) u_0(j, a) da \right] P_i. \quad (\text{A.35})$$

For the matrix B_{ij} from eq. A.1 we can write

$$B_{ij} = \int_{i-1}^{i+1} (1 - |a - i|) u_0(j, a) da. \quad (\text{A.36})$$

Only at the two boundaries $i = 0$ and $i = N$, the upper (respectively lower) boundaries have to be adjusted to 0 and i .

In the rotationally symmetric case, the matrix B needs to be calculated only once for a given system size N and can then be stored for later calculations.

In Fig. 41 you can find a graphical representation of it for $N = 40$. These matrices are well conditioned.

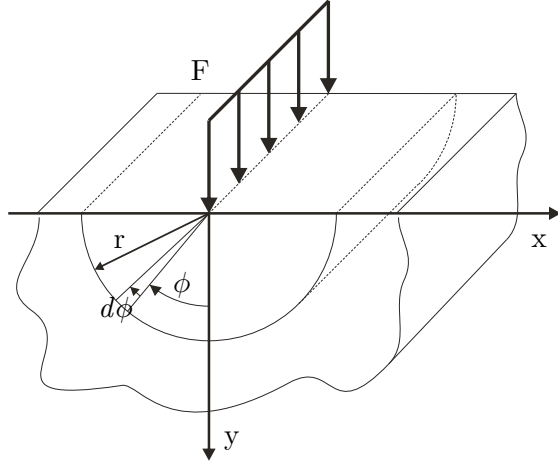


Figure 42: Basic case for the 2D-Boussinesque-solution

2D

The case of 2 spatial dimensions is treated last in this appendix, because of a special difficulty that complicates the calculations. This calculation is needed for any line contact configuration, also in EHL [90]. Again, the underlying equations are from Boussinesque. Consider the case of an infinite line load $\frac{F}{l}$, as in fig. 42.

The deflections in y -direction are given by

$$u(x) = -\frac{F}{l} \frac{(1-\nu^2)}{\pi E} \ln(x^2) + C. \quad (\text{A.37})$$

The force $F(\xi)$ acting at point ξ causes the elementary deflection at point x :

$$u(x) = \frac{1}{\pi E^*} \int_{-\infty}^{\infty} -F(\xi) \ln(x - \xi)^2 d\xi + C. \quad (\text{A.38})$$

In the 2D-case the constant C is generally not known. There is no distinct half-space solution in two spatial dimensions. Let us accept this fact for now and try to bring eq. A.38 into matrix form.

Just as in the radial-symmetric case, we choose $F = \Delta P$ and base functions

$$E_k(x) = \begin{cases} 1 - \frac{|x-x_k|}{\Delta} & \text{for } x_{k-1} \leq x \leq x_{k+1} \text{ and } x_{min} \leq x \leq x_{max} \\ 0 & \text{otherwise} \end{cases}, \quad (\text{A.39})$$

so we get

$$u(x) = \frac{\Delta}{\pi E^*} \int_{-\infty}^{\infty} -\bar{P} \bullet \bar{E}(\xi) \ln(x - \xi)^2 d\xi + C \quad (\text{A.40})$$

$$= \frac{\Delta}{\pi E^*} \left[\int_{-\infty}^{\infty} -\bar{E}(\xi) \ln(x - \xi)^2 d\xi \right] \bullet \bar{P} + C. \quad (\text{A.41})$$

To increase the readability, we will omit the prefactor $\frac{\Delta}{\pi E^*}$ in the following equations.

Again, we consider an evenly spaced grid with $x_i = x_o + i\Delta$. Just as in the radial symmetric case, the integral boundaries are altered and for $u_j = u(x_j)$

$$u_j = \sum_{i=1}^n \left[-2 \int_{x_{i-1}}^{x_{i+1}} \left(1 - \frac{|\xi - x_i|}{\Delta} \right) \ln|x_j - \xi| d\xi \right] P_i + C \quad (\text{A.42})$$

$$= -2 \sum_{i=1}^n \left[\int_{i-1}^{i+1} (1 - |\xi - i|) \ln(\Delta|j - \xi|) d\xi \right] P_i + C \quad (\text{A.43})$$

$$= -2 \left[\sum_{i=1}^n \left[\int_{i-1}^{i+1} (1 - |\xi - i|) \ln(\Delta) d\xi \right] P_i \right. \\ \left. + \sum_{i=1}^n \left[\int_{i-1}^{i+1} (1 - |\xi - i|) \ln(|j - \xi|) d\xi \right] P_i \right] + C. \quad (\text{A.44})$$

The first sum does not depend on j , so we will omit it and say it is included in the constant C which is unknown anyways, so

$$u_j = \sum_{i=1}^n \left[\int_{i-1}^{i+1} (1 - |\xi - i|) \ln(|j - \xi|) d\xi \right] P_i + C \quad (\text{A.45})$$

$$B_{ij} = \int_{i-1}^{i+1} (1 - |\xi - i|) \ln(|j - \xi|) d\xi. \quad (\text{A.46})$$

Again we make sure to have the integral boundaries limited to 1 and N in the first and last addend. All other values B_{ij} only depend on the difference $|i - j|$, so matrix B can be generated very quickly.

An exemplary graphical representation in the case of $N = 40$ can be found in fig. 43 Please note that the first and last column appear smaller than expected. This is because of the limited integration boundaries in these cases. It is intended.

Still we cannot really use this formula in our calculation, because we still have the unknown C . More specifically, our pressure-deflection-dependence in the discrete case

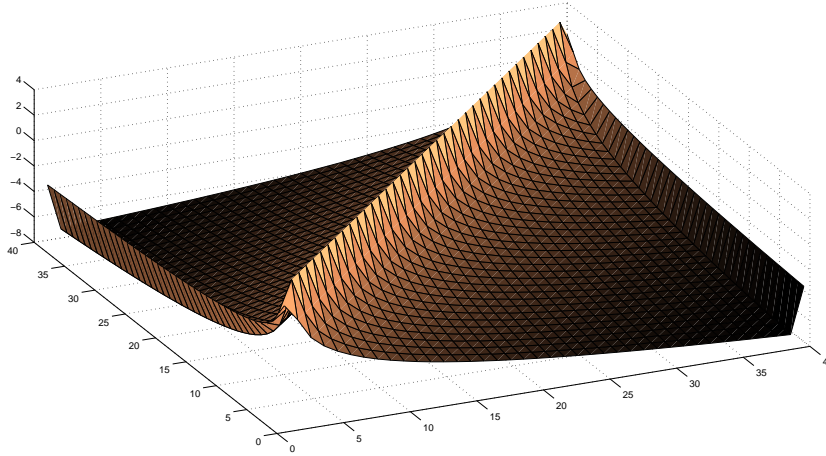


Figure 43: matrix for calculating the surface deflections in the 2D-case., $N = 40$

reads

$$u = A\bar{P} - C. \tag{A.47}$$

This is not all bad, eq. A.47 can still be used for lubricated contact simulations, see for example [73], [46], [75], [24].

A.1.2 Fast integration techniques

In this section, some further methods will be presented, that are not necessary for the understanding of the 3D boundary element method but will greatly reduce the computational cost in a real implementation. We have seen that the matrix in eq. A.1 can easily become very huge. It is a dense (not sparse) matrix, so that we might not even be able to keep it in the computer memory, not to mention solving it. Still the matrix can be described in a parametric way - it is very symmetric and every value can be calculated from its indices. Instead of trying to solve eq. A.1, we will first focus on executing the pure matrix-multiplication $u = Ap$ with given p . Having a fast way of doing it will allow us to introduce iterative solvers to the problem instead of solving it directly. A fast implementation of the 3D deflection from the pressures is also necessary for algorithms, that feature this calculation in an inner iterative loop, such as elastohydrodynamic lubrication simulations [73][10][34].

In the following chapters we will assume a situation where the grid size $N_1 \times N_2$ is so

large that the matrix A (size $N_1 N_2 \times N_1 N_2$) cannot be kept in memory. All procedures will be tailored to fit the 3D BEM, but are equally applicable to the line contact.

Moving-grid-method

This method accelerates the execution of eq. A.8 on computer systems by exploiting both the architecture of modern x86 processors and the regularity of A.15. The so called Kernel represents the basic deformation to the central and all adjacent points resulting from a single, local pressure. This solution is rotational symmetric. In order to obtain all deflections, the following steps must be taken:

For every point $p_{i,j}$, and again for every point $u_{k,l}$, do $u_{k,l} = u_{k,l} + K_{i,j,k,l} \times p_{i,j}$

This has to be executed $N_1^2 \times N_2^2$ times in total. As $K_{i,j,k,l}$ only depends on $|i - k|$ and $|j - l|$, we can simply take A.15 and make it depend only on i and j

$$K2_{ij} = \left[a \ln \frac{c + \sqrt{a^2 + c^2}}{d + \sqrt{a^2 + d^2}} + b \ln \frac{d + \sqrt{b^2 + d^2}}{c + \sqrt{b^2 + c^2}} + c \ln \frac{a + \sqrt{a^2 + c^2}}{b + \sqrt{c^2 + b^2}} + d \ln \frac{b + \sqrt{b^2 + d^2}}{a + \sqrt{a^2 + d^2}} \right] \quad (\text{A.48})$$

by just redefining

$$a = i + \frac{1}{2}, \quad b = i - \frac{1}{2}, \quad c = j + \frac{1}{2}, \quad d = j - \frac{1}{2}. \quad (\text{A.49})$$

We can now store $K2_{ij}$ for $i = -N_1 \dots N_1$ and $j = -N_2 \dots N_2$. The large grayscale rectangle in 44 is a graphical representation of just this matrix. Please note that brightness values are not in scale. Now in order to perform the summation in A.14, the following procedure must be followed. Start with zero deflection. For every pressure point P_{ij} extract the submatrix of $K2$ such that it has the size of the computational area and the $K2_{00}$ value at the ij -spot. Multiply this matrix with P_{ij} and add it to the previous deflections.

For every pressure point ($N_1 \times N_2$ pieces) we have to conduct a scalar-matrix-multiplication and a matrix-addition. In total we have a complexity of $\mathcal{O}(N_1^2 \times N_2^2)$, which means no improvement in terms of complexity!

In practice, you will still see a major acceleration because of these automated matrix-operations are highly optimized with modern computers, so you will see a decrease in computational times by a constant factor and also a great reduction in the memory usage. This method was also used in [39], where the first appearance is said to be [72]. Again, the moving-grid-method is only useful for calculating the surface deflections starting from a given pressure. It cannot be used to solve A.7 directly.

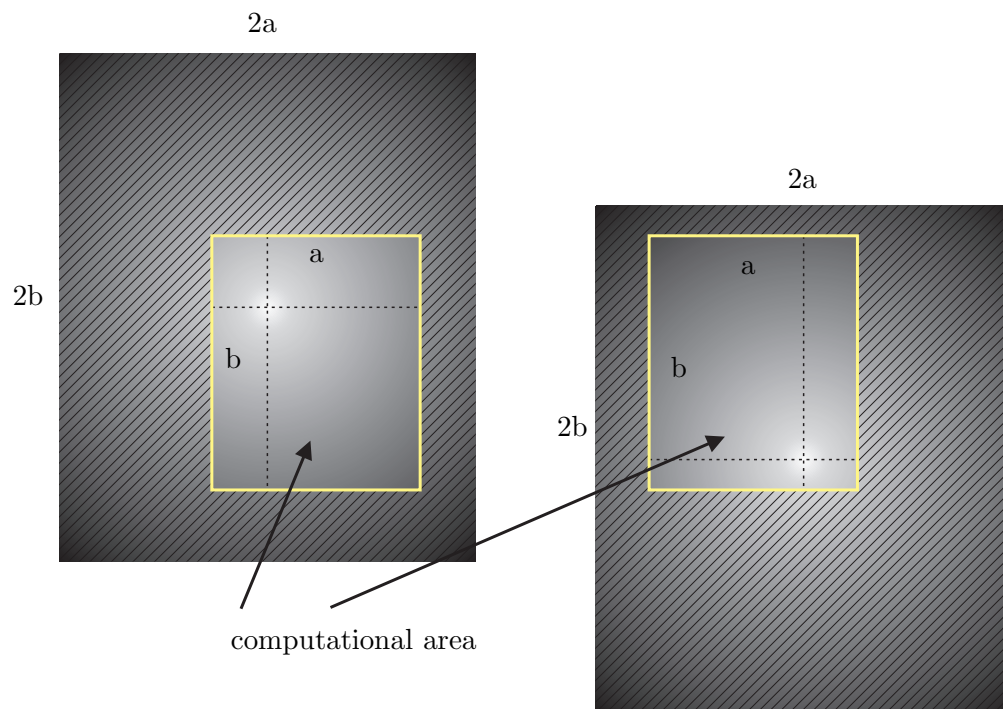


Figure 44: moving-grid-method for acceleration the calculation of surface deflections. Even though the mathematical complexity is not reduced, the performance on current PC systems is greatly improved due to processor architectures and vector operations.

Multi-Level-Multi-Integration

In this section we will look at an elegant and very efficient method for executing the matrix multiplication of A.1. The most important property that we will exploit is the fact that the Kernel matrix K_2 from eq. A.48 is smooth, except in the vicinity of K_{200} . The method was published in [8] and [42] and is described in great detail in [84]. Direct instructions for implementing the method in a computer program can also be found in [64]. In the following, I will present the basic idea according to [84]. Remember we wish to do a large matrix multiplication

$$w_i^h := h^d \sum_j K_{ij}^{hh} w_j^h. \quad (\text{A.50})$$

We will now differentiate between between grid points on the original fin grid x_i^h and those on a grid that is twice as coarse with spacing $H = 2h$. The points are located such that

$$x_{2i}^h = x_i^H. \quad (\text{A.51})$$

We can apply an interpolation to find fine-grid-values starting from coarse-grid-values using

$$w_i^h = \left[II_H^h w^H \right]_i \quad (\text{A.52})$$

Here we use a high-order interpolation II_H^h . The interpolation is done with respect to the index denoted by the dot. For transferring fine-grid-values to the coarse grid, the *transpose* of the interpolation operator, called the anterpolation, is used:

$$\left(II_H^h \right)^T. \quad (\text{A.53})$$

Now let us have a closer look at the Matrix, the Kernel. We assume this Kernel to be smooth, in other words all values can approximately be obtained from interpolation of the surrounding values from the coarse-grid-version

$$K_{i,J}^{hH} := K_{i,2J}^{hh}. \quad (\text{A.54})$$

So we can define an approximate Kernel

$$K_{ij}^{hh} \approx \tilde{K}_{ij}^{hh} := \left[II_H^h K_i^{hH} \right]_j. \quad (\text{A.55})$$

With this Kernel, we can approximate the matrix multiplication to

$$w_i^h \approx \tilde{w}_i^h = h^d \sum_j \tilde{K}_{ij}^{hh} u_j^h = h^d \sum_j \left[II_H^h K_i^{hH} \right]_j u_j^h. \quad (\text{A.56})$$

As the interpolation II_H^h is a real matrix, its transpose is also its adjoint matrix. We can thus replace the sum by

$$\tilde{w}_i^h = h^d \sum_J K_{iJ}^{hH} \left[\left(II_H^h \right)^T u^h \right]_J = H^d \sum_J K_{iJ}^{hH} u_J^H \quad (\text{A.57})$$

with

$$u_J^H := 2^{-d} \left[\left(II_H^h \right)^T u^h \right]_J. \quad (\text{A.58})$$

In this form, we only need to execute a sum over the capital J elements in the coarse grid – a 2^d -times smaller number. In order to do so, we only have to replace u by its scaled and antepolated coarse-grid version u_J^H and use the interpolated kernel. The same procedure can be applied recursively to even coarser grids.

One problem remains; the Kernel as given by eq. A.15 is not smooth in the vicinity of K_{00} . This problem can be solved by predetermining the exact error done by assuming its smoothness and correcting it in the vicinity of each pressure value. Doing so will increase the computational effort by a considerable factor, but will not alter the reduced complexity. No assumptions regarding u have been made, only the smoothness property of the Kernel is needed. Therefore, the procedure can also be applied to other Kernels, such as the basic deflection resulting from a single, *tangential* force. Again, see [42],[84] and [64] for details. It shall be noted that the Multi-Level-Multi-Integration was one of the key ingredients that led to the success of this current work, but later was dropped because the fast convolution method proved to be far more efficient.

Fast Convolution using FFT

Another way to execute the matrix multiplication is to view eq. A.13 as a convolution of two 2-dimensional functions

- the pressures $p(x, y)$
- the kernel $\frac{1}{R}$

Now in order to find the deflections resulting from a given pressure distribution, we can make a the convolution an element-wise multiplication in Fourier-space and apply the inverse transform

$$u_z(x, y) = \frac{1}{\pi E^*} FFT T^{-1} \left[FFT(p) \cdot FFT\left(\frac{1}{R}\right) \right]. \quad (\text{A.59})$$

In order to account for the free boundaries, it is necessary to choose the computational domain of the FFT twice as big as the physical domain.

The method was described in [80] and [15]. It outperforms the two previously mentioned methods for two reasons

- It is very easy to implement, resulting in less than ten lines of computer code
- Very efficient implementations of (also the more-dimensional) FFT exist for almost all hardware platforms. At the time of the writing of this thesis, the best choice was to use *General Purpose Graphics Processing Units*, as from NVIDIA (Cuda) or ATI (ATI-Stream), thereby increasing execution speed by a factor of roughly 100 compared to CPU-based computing.

A Comparison of the fast convolution to MLMI is given in [86] and authors find the the FFT-based method to be fastest, even though the advantage of using highly optimized parallel routines for the FFT is not yet taken into account. As for the MLMI, the fast convolution algorithm can equally be applied to other kernels, such as the Cerrutti-solution for tangential loading.

A.1.3 Iterative procedures

The aim is to find a solution to A.7, where some deflections are given and the pressure is unknown that leads to this deflection. All points are coupled depending on their original distance in the computational grid. If the system size is small, we can keep the whole system matrix in memory, pass it over to some solver that we deem suitable and forget about the problem. Two problems arise here. First, the matrix is full (not sparse) and is likely to be too big to be kept in memory and second it is positive definite but not diagonal-dominant, so we cannot freely choose a solver. If on the other hand, there is

an efficient way to execute the matrix-*multiplication* of eq. A.1, then we use it to solve the linear equation system using an iterative procedure. One way to do this is described in [84], but his methodology does not guarantee convergence due to the local relaxation step. In contrast Polonsky and Keer [64] use the CG-method and find convergence for arbitrary surfaces. Lets us have a look at this procedure in more detail.

In the last section we have seen different ways to quickly execute the matrix-multiplication of A.1. Lets assume we have chosen one of the procedures mentioned there, such that $u = Ap$ with any given p can be executed without reaching memory or time limitations. The linear system can now be solved using a suitable iterative scheme. The conjugate gradients method is a good choice, because it converges rapidly and only demands for the underlying matrix to be positive definite and symmetric. In order to find p from u , one must [88]

- choose any $p_0 \in \mathbb{R}^n$
- calculate $r_0 = u - Ap_0$ and set $d_0 = r_0$
- repeat until the residual is below a given tolerance $\|r_{k+1}\| < tol$
 - starting from p_k , find p_{k+1} in direction d

$$p_{k+1} = p_k + \frac{r_k^T r_k}{d_k^T d_k} d_k$$

$$r_{k+1} = r_k - \alpha_k d_k$$
 - correct the direction d_k

$$d_{k+1} = r_{k+1} + \frac{r_{k+1}^T r_{k+1}}{r_k^T r_k} d_k$$

Even though the MLMI and FFT methods both use the whole computational domain as input and output, they can be used on a subset of grid points. In A.1 we have seen that often times we wish to find the pressures *inside the assumed contact area* as a function of the deflections *only inside the assumed contact area*. This problem can easily be solved by setting the pressures zeros outside the area of contact to zero. After the fast multiplication is done, all deflections outside this area are discarded.

For example, lets say we wish to find the contact stiffness of a given contact configuration, that is the partitioning in zones of contact / no contact. Using the above CG-methodology this can easily be done

- set all $u_i = 1L$ inside the contact area

- find the corresponding pressure p_i using the CG-method

- determine the resulting force as

$$F = \Delta_x \Delta_y \sum_i p_i$$

- find the stiffness as

$$k = \frac{F}{1L}$$

Where $1L$ is an arbitrary non-zero length and Δ_x, Δ_y are the grid spacing constants.

A.2 1D Method of Dimensionality Reduction

The Method of Dimensionality Reduction is a tool that allows for a radically different approach to contact problems than most other numerical methods. There are two parts to this method. The first is to substitute a three-dimensional contact problem to a corresponding one-dimensional contact problem using a set of theorems. The second step is to solve this new system, which can be done analytically in many cases or require numerical methods, depending on the complexity and the effects that should be modeled

Finding a corresponding 1D system

The basic idea of the reduction of contact system from three dimensions to one has been published in numerous papers, mainly by Prof. V. Popov and co-workers [22], [21], [68], [66], [69] and more recently by Scaraggi et. al. [74]. An excellent overall summary of the method, it's basic properties, applications and open questions can be found in [65]. Furthermore, there is a very recent book covering the topic extensively [67]. Therefore I only wish to give the basic idea presented in [21] for any reader whose first encounter with the method of dimensionality reduction is this current work.

In the following section, I will limit myself to the elastic normal contact, following all assumptions presented in 1. The basic claim for the elastic contact problem is the following:

A given threedimensional contact problem can be mapped onto an equivalent onedimensional system, while preserving all interdependencies between normal force F_N , indentation depth d , contact stiffness k_N , and contact radius (where applicable). The three dimensional system has the property of elastic coupling between all surfaces points according to A.13, while in the one-dimensional system, no coupling applies.

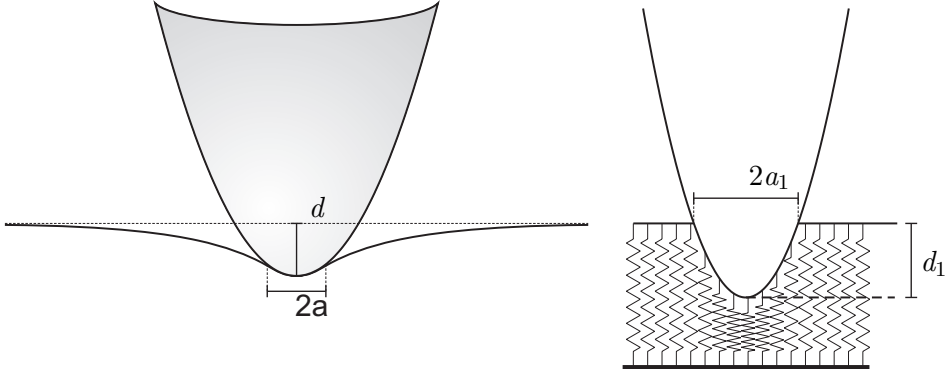


Figure 45: (a) basic Hertzian contact in 3 dimensions. (b) equivalent reduced contact problem in 1D. The foundation of springs should be viewed as densely packed.

The independence of surface points in the onedimensional system is often associated with the term *Winkler-foundation* and can be imagined as very fine set of densely aligned independent linear springs. The most prominent example to illustrate this transformation is the case of the Hertzian contact. A spherical stiff indenter with radius R (approximated by the shape $z(r) = r^2/2R$) is pushed into the elastic half space, see fig. 45(a). From Hertz' classical paper [31] we know the following dependencies

$$F_N = \frac{4}{3} E^* \sqrt{R} d^{3/2}, \quad (\text{A.60})$$

$$a = \sqrt{Rd}. \quad (\text{A.61})$$

In the linear 1D case of no interactions between the elastic elements and $z_1(x) = x^2/2R_1$ it can be seen that there is a simple geometric condition

$$a = \sqrt{2R_1 d}. \quad (\text{A.62})$$

Now imagine the springs in 45(b) to be densely but equally spaced with the distance Δx between them. Let the effective stiffness of each spring be

$$\Delta k_N = E^* \Delta x. \quad (\text{A.63})$$

The overall stiffness of the indented system is simply the length of contact multiplied with the effective stiffness

$$k_N = 2aE^*. \quad (\text{A.64})$$

The normal force can be found by summing (or integrating) all spring deflections times the effective single stiffness, giving

$$F_N = \frac{4\sqrt{2}}{3} E^* \sqrt{R_1} d^{3/2}. \quad (\text{A.65})$$

So simply by choosing

$$R_1 = \frac{R}{2}, \quad (\text{A.66})$$

we can find that eq. A.61 and A.62 as well as A.60 and A.65 coincide.

In the Hertzian case, it is thus very simple to find the equivalent reduced system. In fact, all radially symmetric indenters of different shapes can be transformed in a quite simple and compelling way, as was proven in [28] and [29], as long as the resulting contact area is a circle, as opposed to multiple rings.

Finding a corresponding reduced system for rough surfaces

Again, the content of this section can be found in either [65] or [67] in greater detail. It is also part of [63] and [60]. The question to be answered is how to find an equivalent one-dimensional system if the original system is not a single radially symmetric indenter, but a rough surface. Let the rough surface be defined by its power spectrum

$$C_{2D}(\bar{q}) = \frac{1}{(2\pi)^2} \int \langle f(\bar{x}) f(0) \rangle \exp(i\bar{x}\bar{q}) d\bar{x}. \quad (\text{A.67})$$

The surface can be calculated using

$$h(\bar{x}) = \int_{q_{\min}}^{q_{\max}} dq B_{2D}(\bar{q}) \cos(\bar{q}\bar{x} + \phi(\bar{q})), \quad (\text{A.68})$$

$$B_{2D}(\bar{q}) = \frac{2\pi}{L} \sqrt{C_{2D}(\bar{q})}. \quad (\text{A.69})$$

We will further assume the surface to be isotropic, in other words, the power spectrum may only depend on the length of the wave vector, not on its orientation. As we assume random roughness, we require for the phases ϕ to be randomly distributed.

The one-dimensional system that we are looking for an equivalent rough line. Such a

line can be rebuilt from the spectral density too, this time

$$h(x) = \int_{q_{\min}}^{q_{\max}} dq B_{1D}(q) \cos(qx + \phi(q)), \quad (\text{A.70})$$

$$B_{1D}(q) = \sqrt{\frac{2\pi}{L} C_{1D}(q)}. \quad (\text{A.71})$$

We need the relation between C_{2D} and C_{1D} that gives the same properties in contact mechanics. In [65] it is argued that such a transformation must be of the form

$$C_{1D} = \int_q^\infty C_{2D}(q') K(q, q') dq', \quad (\text{A.72})$$

with $K(q, q')$ a homogenous function of zero order, which has not been found yet. Much earlier in [22] a much simpler form was given

$$C_{1D} = \pi q C_{2D}. \quad (\text{A.73})$$

This was initially motivated by the idea that both the 1D and 3D surface should give the same rms roughness, which reads in the 1D and 3D case respectively:

$$\langle h^2 \rangle_{2D} = 2\pi \int_0^\infty q C_{2D}(q) dq, \quad (\text{A.74})$$

$$\langle h^2 \rangle_{1D} = 2 \int_0^\infty C_{1D}(q) dq. \quad (\text{A.75})$$

In [67] it is shown that in the case of discrete surfaces generated by means of iFFT (sec. 2.3.2), the prefactor in eq. A.73 is not constant π but depends on both H and the discrete system size N , according to

$$\lambda(H) = \frac{1}{2} \frac{\sum_{n=-N, m=-N}^N \frac{1}{(n^2+m^2)^{H+1}}}{\sum_{n=-N}^N \frac{1}{|n|^{2H+1}}}. \quad (\text{A.76})$$

See fig. 46.

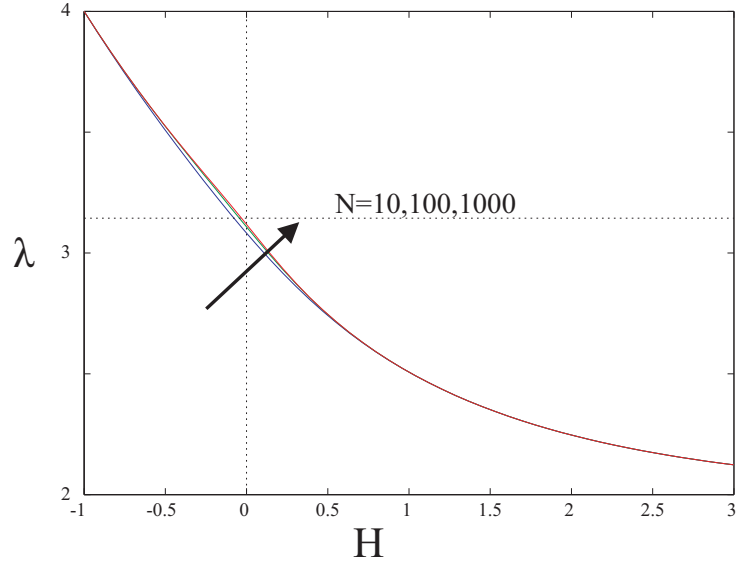


Figure 46: For discrete self-affine surfaces, the prefactor in eq. A.73 actually differs from π . It only approaches π for $H = 1$ and a large number of grid points N . See [67] for details.

Solving a reduced system

In any one-dimensional system, the normal force F as well as the normal contact stiffness k can easily be found as a function of the *indentation depth* d . This is because for a known value of d , both can easily be evaluated, see fig. 47. Numerically speaking, it is not a complicated thing to find and count the number of springs in contact and to sum up all their deflections. When one is interested in finding the stiffness value starting from a given normal force, then one must first find the corresponding indentation depth, for example using binary search, which can be time-consuming, especially if the aim is to find a series of stiffness values for some given force values. One way to facilitate the evaluation is to sort the discrete numerical values by their height, see fig. 48.

Let N be the number of points of the rough line and m be the number of force values you wish to evaluate. Then the original complexity of performing the binary search $\mathcal{O}(\log(N) N \cdot m)$ can be reduced to $\mathcal{O}(\log(N) N)$. In doing so, we exploited the independence of the springs and thus let go of their neighboring relations. This must not be done, when these neighboring relations actually play a significant role, as in the adhesive contact, see [67] for details.

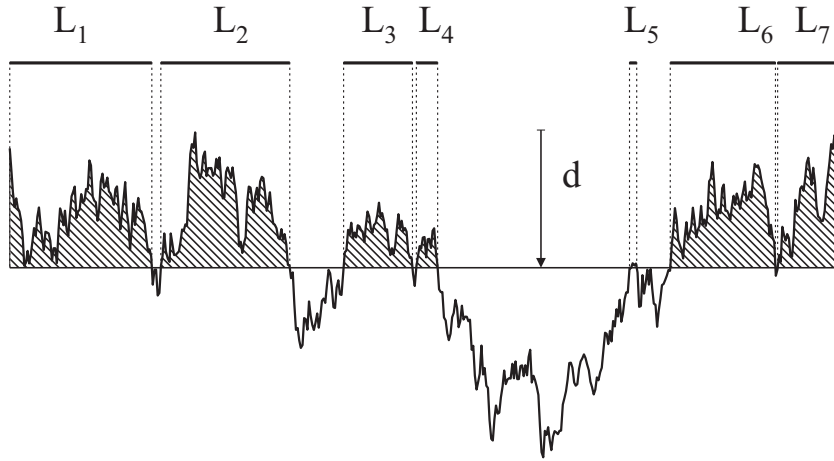


Figure 47: Interpretation of the indentation of a 1D rough line. The overall stiffness is the sum of springs in contact $k = \frac{E^*}{n} \sum_i L_i$ and the normal force is the shaded area $F_N = E^* \Delta \sum_c (h_c - d)$, where h_c are the positions of the springs in contact and Δ is the grid spacing.

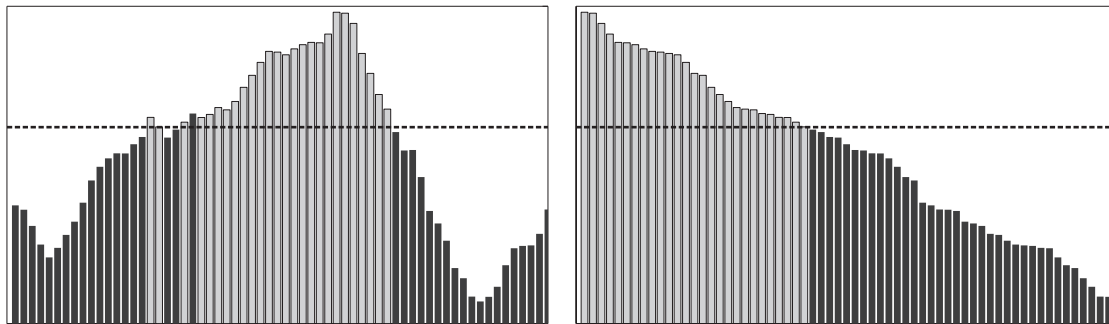


Figure 48: The evaluation of a discrete rough line can be facilitated by sorting the numerical array prior to the indentation. In this way, finding the appropriate indentation depth for a given normal force can be done much faster.

References

- [1] S. AKARAPU, T. SHARP, AND M. O. ROBBINS. Stiffness of contacts between rough surfaces. *Phys. Rev. Letters* **106/204301**, 1–4 (2011).
- [2] F. ARCHARD. Contact and rubbing of flat surfaces. *Journal Of Applied Physics* **24**, 981–988 (1953).
- [3] D. AVNIR, D. FARIN, AND P.PFEIFER. Molecular fractal surfaces. *Nature* **308**, 261–263 (1984).
- [4] J. BARBER. Bounds on the electrical resistance between contacting elastic rough bodies. *Proceedings of the Royal Society London* **A459**, 53–60 (2003).
- [5] J. R. BARBER. Incremental stiffness and electrical contact conductance in the contact of rough finite bodies. *Phys. Rev. E* **87 / 013203**, 1–5 (2013).
- [6] B. BHUSHAN AND A. MAJUMDAR. Role of fractal geometry in roughness characterization and contact mechanics of surfaces. *Journal of tribology* **112**, 205–216 (1990).
- [7] M. BORRI-BRUNETTO, B.CHIAIA, AND M. CIAVARELLA. Incipient sliding of rough surfaces in contact: a multiscale numerical analysis. *Computer methods in applied mechanics and engineering* **190**, 6053–6073 (2001).
- [8] A. BRANDT AND A. LUBRECHT. Multilevel matrix multiplication and fast solution of integral equations. *Journal of Computational Physics* **2**, 348–370 (1990).
- [9] M. BRAUNOVIC, V. V. KONCHITS, AND N. K. MYSHKIN. “Electrical Contacts”. CRC Press (2007).
- [10] S. BUKOVNIK, N. DÖRR, V. CAIKA, W. J. BARTZ, AND B. LOIBNEGGER. Analysis of diverse simulation models for combustion engine journal bearings and the influence of oil condition. *Tribology International* **39(8)**, 820 – 826 (2006).
- [11] A. BUSH AND R. GIBSON. a theoretical investigation of thermal contact conductance. *Applied Energy* **5/1**, 11–22 (1979).
- [12] A. BUSH, R. GIBSON, AND T. THOMAS. The elastic contact of a rough surface. *Wear* **35**, 87–112 (1975).

- [13] R. BUZIO, C. BORAGNO, F. BISCARINI, F. B. DE MONGEOT, AND U. VALBUSA. The contact mechanics of fractal surfaces. *Nature Materials* **2**, 233–236 (April 2003).
- [14] C. CAMPANA, B. PERSSON, AND M. MÜSER. Transverse and normal interfacial stiffness of solids with randomly rough surfaces. *Journal of physics: condensed matter* **23**, 1–9 (2011).
- [15] Y.-J. CHO, Y.-P. KOO, AND T.-W. KIM. A new fft technique for the analysis of contact pressure and subsurface stress in a semi-infinite solid. *KSME International Journal* **14/3**, 331–337 (2000).
- [16] M. CIAVARELLA, V. DELFINE, AND G. DEMELIO. A "re-vitalized" greenwood and williamson model of elastic contact between fractal surfaces. *Journal of the Mechanics and Physics of Solids* **54**, 2569–2591 (2006).
- [17] M. CIAVARELLA, J. GREENWOOD, AND M. PAGGI. Inclusion of interaction in the greenwood and williamson contact theory. *Wear* **265**, 729–734 (2008).
- [18] M. G. COOPER, B. B. MIKIC, AND M. M. YOVANOVICH. Thermal contact conductance. *International Journal of Heat and Mass Transfer* **12**, 279–300 (1969).
- [19] H. DYER, D. AMITRANO, AND A.-M. BOULLIER. Scaling properties of fault rocks. *Journal of Structural Geology* **45**, 125–136 (2012).
- [20] L. GALIN. Contact problems in the theory of elasticity. *Gostekhizdat Moscow* (1953).
- [21] T. GEIKE. "Theoretische Grundlagen eines schnellen Berechnungsverfahrens für den Kontakt rauer Oberflächen". Dissertation, TU-Berlin (2007).
- [22] T. GEIKE AND V. POPOV. Mapping of three-dimensional contact problems into one dimension. *Phys. Rev. E* **76** / **036710**, 1–5 (2007).
- [23] G. E. GLADWELL. "Contact Problems - The legacy of L.A. Galin", vol. 155 of "Solid Mechanics and Its Applications". Springer (2008).
- [24] R. GOHAR. "Elastohydrodynamics". Imperial College Press, 2 ed. (2001).
- [25] J. GREENWOOD AND J. WILLIAMSON. Contact of nominally flat surfaces. *Proceeding of the Royal Society* **A295**, 300 (1966).
- [26] J. A. GREENWOOD. Constriction resistance and the real area of contact. *British Journal of Applied Physics* **17/12**, 1621–1632 (1966).

- [27] B. GRZEMBA, R. POHRT, E. TEIDELT, AND V. L. POPOV. Maximum micro-slip in tangential contact of randomly rough self-affine surfaces. *Wear* **accepted**, 1–5 (2013).
- [28] M. HESS. “Über die exakte Abbildung ausgewählter dreidimensionaler Kontakte auf Systeme mit niedrigerer räumlicher Dimension”. Cuvillier-Verlag, Göttingen (2011).
- [29] M. HESS. On the reduction method of dimensionality: The exact mapping of axisymmetric contact problems with and without adhesion. *Physical Mesomechanics* **15**, 264–269 (2012).
- [30] J. M. HERRMANN. “Physikalische Grenzen von optischen 3D-Sensoren”. PhD thesis, Friedrich-Alexander-Universität Erlangen-Nürnberg (1994).
- [31] H. HERTZ. Über die berührung fester elastischer körper. *Journal für die reine und angewandte Mathematik* **92**, 156–171 (1881).
- [32] S. HYUN, L. PEI, J.-F. MOLINARI, AND M. O. ROBBINS. Finite-element analysis of contact between elastic self-affine surfaces. *Physical Review* **E70**, 026117 (2004).
- [33] S. HYUN AND M. O. ROBBINS. Elastic contact between rough surfaces: Effect of roughness at large and small wavelengths. *Tribology International* **40**, 1413–1422 (2007).
- [34] G. KNOLL. Elasto-hydrodynamische simulationstechnik mit integriertem mischreibungskontakt. *Materialwissenschaft und Werkstofftechnik* **34**, 946–952 (2003).
- [35] K. KOMVOPOULOS AND N. YE. Three-dimensional contact analysis of elastic-plastic layered media with fractal surface topographies. *Journal of Tribology* **123.3**, 632–641 (2001).
- [36] S. KÜRSCHNER AND V. L. POPOV. Penetration of self-affine fractal rough rigid bodies into a model elastomer having a linear viscous rheology. *Phys. Rev. E* **E 87**, **042802**, 1–5 (2013).
- [37] B. LAACKMAN. “Beitrag zur fraktalen Beschreibung technischer Oberflächen”. PhD thesis, Universität hannover (1996).
- [38] E. H. LEE. *Quart. Appl. Math* **13/183** (1955).

- [39] M. LEIDNER. “Kontaktphysikalische Simulation von Schichtsystemen”. PhD thesis, Technische Universität Darmstadt (Mai 2009).
- [40] Q. LI, M. POPOV, A. DIMAKI, A. FILIPPOV, S. KÜRSCHNER, AND V. POPOV. Friction between a viscoelastic body and a rigid surface with random self-affine roughness. *Phys. Rev. Letters* **111/034301**, 5 (2013).
- [41] B. LORENZ AND B. N. J. PERSSON. Interfacial separation between elastic solids with randomly rough surfaces: comparison of experiment with theory. *Journal of Physics, Condens. Matter* **21**, 1–6 (2009).
- [42] A. A. LUBRECHT AND E. IOANNIDES. A fast solution of the dry contact problem and the associated sub-surface stress field, using multilevel techniques. *ASME Journal of Tribology* **113**, 128–133 (1991).
- [43] W. MANNERS AND J. GREENWOOD. Some observations on persson’s diffusion theory of elastic contact. *Wear* **261**, 600–610 (2006).
- [44] G. S. MILLER. The definition and rendering of terrain maps. *Computer Graphics* **20/4**, 39–48 (1986).
- [45] R. MINDLIN. Compliance of elastic bodies in contact. *ASME Journal of applied mechanics* **16**, 259–262 (1949).
- [46] D. A. MOHRENSTEIN-ERTEL. Die berechnung der hydrodynamischen schmierung gekrümmter oberflächen unter hoher belastung und relativbewegung. Fortschrittsberichte der VDI-Zeitschriften 115, Verein Deutscher Ingenieure (1984).
- [47] B. NIKOLIC AND P. B. ALLEN. Electron transport through a circular constriction. *Phys. Rev. B* **60**, 3963–3969 (1999).
- [48] D. NOLBERT AND Z. RYMUZA. Frictional and adhesive and adhesive interactions at the interface mold-resist in nanoimprint lithography process. In “German-Russian Workshop, Friction: From elementary mechanisms to macroscopic behavior TUB October 16-17” (2012).
- [49] G. NOPPEN AND J. SIGALLA. “Technische Oberflächen - Oberflächenbeschaffenheit”. Beuth Verlag (1985).
- [50] M. PAGGI AND J. BARBER. Contact conductance of rough surfaces composed of modified rnd patches. *International Journal of Heat and Mass Transfer* **54**, 4664–4672 (2011).

- [51] L. PASTEWKA, N. PRODANOV, B. LORENZ, M. H. MÜSER, M. O. ROBBINS, AND B. N. J. PERSSON. Finite-size scaling in the interfacial stiffness of rough elastic contacts. *Phys. Rev. E* **87** / **062809**, 1–9 (2013).
- [52] B. PERSSON. Elastoplastic contact between randomly rough surfaces. *Phys. Rev. Lett.* **87**(11), 116101 (Aug 2001).
- [53] B. PERSSON. Theory of rubber friction and contact mechanics. *Journal of Chemical Physics* **115**/5, 3840–3861 (2001).
- [54] B. PERSSON. Contact mechanics for randomly rough surfaces. *Surface Science Reports* **61**, 201–227 (2006).
- [55] B. PERSSON. Relation between interfacial separation and load: A general theory of contact mechanics. *Physical Review Letters* **99**/125502, 1–4 (2007).
- [56] B. PERSSON. Multiscale contact mechanics. In “German Russian Workshop, Friction: ‘From elementary mechanisms to macroscopic behavior’ at Technische Universität Berlin” (10 2012).
- [57] B. PERSSON, O. ALBOHR, U. TARTAGLINO, A. I. VOLOKITIN, AND E. TOSATTI. On the nature of surface roughness with application to contact mechanics, sealing, rubber friction and adhesion. *J. Phys.: Condens. Matter* **17**, 1–62 (2004).
- [58] R. POHRT AND V. POPOV. Contact stiffness of randomly rough surfaces. *Scientific Reports* **3** / **3293**, 1–6 (2013).
- [59] R. POHRT AND V. L. POPOV. Contact mechanics of randomly rough self-affine surfaces. (2012).
- [60] R. POHRT AND V. L. POPOV. Investigation of the dry normal contact between fractal rough surfaces using the reduction method, comparison to 3d simulations. *Physical Mesomechanics* **15**, N. 5-6, 275–279 (2012).
- [61] R. POHRT AND V. L. POPOV. Normal contact stiffness of elastic solids with fractal rough surfaces. *Physical Review Letters* **108**, **104301**, 1–4 (2012).
- [62] R. POHRT AND V. L. POPOV. Contact mechanics of rough spheres: Crossover from fractal to hertzian behavior. *Advances in Tribology* **2013**/974178, 1–4 (2013).

- [63] R. POHRT, V. L. POPOV, AND A. E. FILIPPOV. Normal contact stiffness of elastic solids with fractal rough surfaces for one- and three-dimensional systems. *Physical Review E* **86**, 026710, 1–7 (2012).
- [64] I. POLONSKY AND L. KEER. A numerical method for solving rough contact problems based on the multi-level multi-summation and conjugate gradient techniques. *Wear* **231**, 206–219 (1999).
- [65] V. POPOV. Method of reduction of dimensionality in contact and friction mechanics: A linkage between micro and macro scales. *Friction* **1**, 41–62 (2013).
- [66] V. POPOV AND A.E.FILIPPOV. Force of friction between fractal rough surface and elastomer. *Tech. Phys. Lett.* **36/9**, 525–527 (2010).
- [67] V. POPOV AND M. HESS. “Methode der Dimensionsreduktion in Kontaktmechanik und Reibung. Eine Berechnungsmethode im Mikro- und Makrobereich”. Springer (2013).
- [68] V. POPOV AND S. PSAKHIE. Numerical simulation methods in tribology. *Tribology International* **40**, 916–923 (2007).
- [69] V. L. POPOV. “Contact Mechanics and Friction. Physical Principles and Applications”. Springer (2009).
- [70] V. L. POPOV. “Kontaktmechanik und Reibung. Von der Nanotribologie bis zur Erdbebendynamik”. Springer (2009).
- [71] J. R. M. RADOK. *Quart. Appl. Math* **15/198** (1957).
- [72] N. REN AND S. LEE. Contact simulation of three dimensional rough surfaces using moving grid methods. *ASME Jour. Of Trib* **15**, 597–601 (1993).
- [73] M. SARANGI. “On The Dynamics Of Lubricated Ball Bearings”. PhD thesis, Indian Institute of Technology (2005).
- [74] M. SCARAGGI, C. PUTIGNANO, AND G. CARBONE. Elastic contact of rough surfaces: A simple criterion to make 2d isotropic roughness equivalent to 1d one. *Wear* **297**, 811–817 (2013).
- [75] M. SCHOLLE. Hydrodynamical modelling of lubricant friction between rough surfaces. *Tribology International* **40**, 1004–1011 (2007).

- [76] C. H. SCHOLZ. The critical slip distance for seismic faulting. *Nature* **336**, 761–763 (1988).
- [77] C. SEGEDIN. The relation between load and penetration for a spherical punch. *Mathematica* **4**, 156–161 (1957).
- [78] I. N. SNEDDON. The relation between load and penetration in the axisymmetric boussinesq problem for a punch of arbitrary profile. *International Journal of Engineering Science* **3**, 47–57 (1965).
- [79] H. SORG. “Praxis der Rauheitsmessung und Oberflächenbeurteilung”. Carl Hanser Verlag (1995).
- [80] H. M. STANLEY AND T. KATO. An fft-based method for rough surface contact. *Journal of Tribology* **119(3)**, 481–485 (1984).
- [81] E. TEIDELT, E. WILLERT, A. FILIPPOV, AND V. POPOV. Modeling of the dynamic contact in stick-slip microdrives using the method of reduction of dimensionality. *Physical Mesomechanics* **15 N. 5-6**, 287–292 (2012).
- [82] R. S. TIMSIT. Electrical contact resistance: Properties of stationary interfaces. *IEEE Transactions on components and packaging technologies* **22(1)**, 85–98 (March 1999).
- [83] R. S. TIMSIT. Electrical contact resistance: Properties of stationary interfaces. *IEEE Transactions on Components and Packaging Technology* **2**, 85–98 (1999).
- [84] C. VENNER AND A. LUBRECHT. “Multilevel Methods in Lubrication”. Elsevier Tribology Series, 37 (2000).
- [85] S. WANG AND K. KOMVOPOULOS. A fractal theory of the interfacial temperature distribution in the slow sliding regime: Part 1 - elastic contact and heat transfer analysis. *Transactions of the ASME* **116**, 812–823 (1994).
- [86] W. WANG, H. WANG, Y.-Z. H. Y.C. LIU, AND D. ZHU. A comparative study of the methods for calculation of surface elastic deformation. *Proceedings of the Institution of Mechanical Engineers, Part J: Journal of Engineering Tribology* **217**, 145–153 (2003).
- [87] R. WETTER. Numerische berechnung des elektrischen engewiderstands im kontakt rauer oberflächen. Master’s thesis, Technische Universität Berlin, Prof. V.Popov (2011).

- [88] P. D. WIKIPEDIA. Cg-verfahren. online (09 2013).
- [89] P. D. WIKIPEDIA. Entfernungsmessung. online (09 2013).
- [90] M. WISNIEWSKI. “Elastohydrodynamische Schmierung”. No. 9 in Handbuch der Tribologie und Schmierungstechnik. expert verlage (2000).
- [91] M. M. YOVANOVICH. Four decades of research on thermal contact, gap, and joint resistance in microelectronics. *IEEE Transactions on Components and Packaging Technology* **28/2**, 182–206 (2005).
- [92] G. ZAVARISE, M. BORRI-BRUNETTO, AND M. PAGGI. On the reliability of microscopical contact models. *Wear* **257**, 229–245 (2004).
- [93] G. ZAVARISE, M. BORRI-BRUNETTO, AND M. PAGGI. On the resolution dependence of micromechanical contact models. *Wear* **262**, 42–54 (2007).